SENSE & SUSCEPTIBILITY: RESPIRATION-RELATED SUSCEPTIBILITY EFFECTS AND THEIR INTERACTIONS WITH PARALLEL IMAGING

By

John Sexton

Thesis

Submitted to the Faculty of the

Graduate School of Vanderbilt University

in partial fulfillment of the requirements

for the degree of

MASTER OF SCIENCE

in

Biomedical Engineering

December, 2006

Nashville, Tennessee

Approved:

Dr. John Gore

Dr. Chris Gatenby

To my parents, who always provide encouragement and perspective

And

To Zea Miller, who constantly surprises me with her love and support

ACKNOWELDGMENTS

I would like to thank Dr. John Gore and Dr. Chris Gatenby for their guidance and feedback. Research presented here was funded by the National Science Foundation as part of the National Science Foundation Graduate Research Fellowship Program.

TABLE OF CONTENTS

Page

Appendix

LIST OF FIGURES

CHAPTER I

INTRODUCTION

Medical Imaging

Modern medicine depends on the ability to image the human body. Diagnosis, surgical planning and functional imaging enhance ability to treat human illness without expensive and potentially dangerous invasive medical procedures. The brain in particular is delicate and complex, making non-invasive imaging techniques especially important. Prominent forms of medical imaging today include X-Ray and Computed Tomography (CT), Nuclear Medicine and Positron Emission Tomography (PET), Ultrasound, and Magnetic Resonance Imaging (MRI). Each method has intrinsic strengths and weaknesses and is individually suited to providing anatomic and/or functional data. Figure 1 shows brain images generated by each modality.

X-Ray (a) and CT (b) images clearly show bone, but because X-rays do not attenuate well in soft tissue these modalities do not produce detailed images of brain tissue. PET (c) images show areas of increased blood flow but provide no soft tissue contrast (pixels of higher activity are red). Ultrasound (d) images can be produced quickly but fail to capture anatomical detail because ultrasound image contrast is derived from backscatter, which does not work well with a physically intricate organ such as the brain.

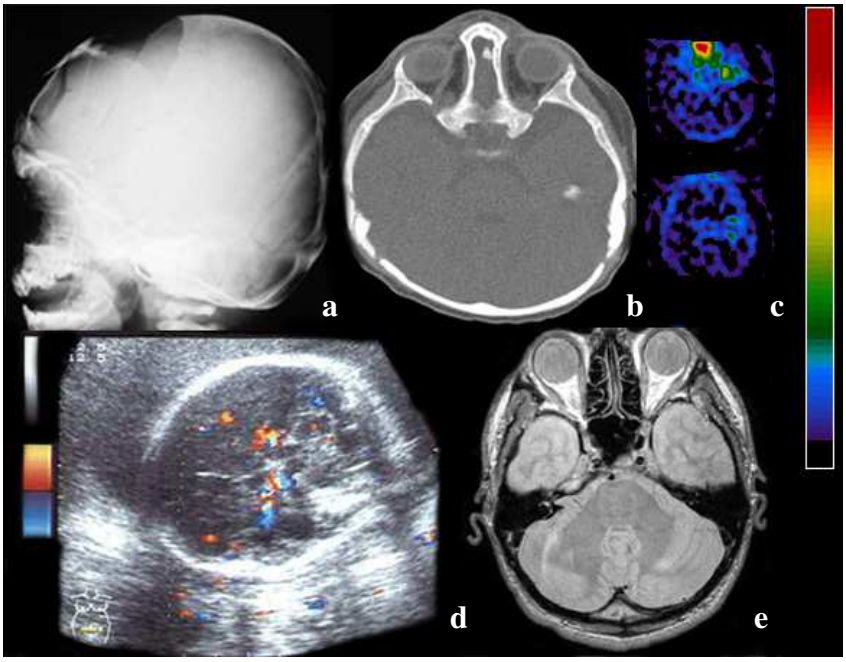

Figure 1. Brain images with a) X-Ray b) Computed Tomography c) Nuclear Medicine (PET) d) Ultrasound e) Magnetic Resonance Imaging
Images: www.ob-ultrasound.net; http://www.uke.uni-hamburg.de; http://www.med.harvard.edu

Ultrasound is better suited to measuring blood velocity in blood vessels; here, blood vessels are red and blue. MRI (e) has emerged as one of the most powerful and flexible imaging techniques to date, producing both detailed, high contrast images of soft tissue as well as functional information.

MRI utilizes the single-proton hydrogen nucleus—primarily those found in soft tissue water—to image the human body with full three-dimensional capabilities, excellent soft-tissue contrast, and high spatial resolution (~1 mm). The human body, including the brain, is approximately 70% water, found in different tissues in varying amounts. MRI contrasts soft tissues such as gray matter, white matter, and brain tumor without the need for exogenous contrast agents or ionizing radiation; it is therefore well-suited to imaging the human body, particularly the brain (Webb 2003).

Clinical diagnoses using MRI generally rely on the intrinsic contrast between pathological and healthy tissue. The detection of brain disease depends mainly on the changes in relaxation times associated with cellular damage. In brain tumors, there is often an increase in water concentration, so the tumor shows up as an area of higher signal intensity than the surrounding tissue on an MR image that depicts proton density.

Irrespective of the method used to acquire medical images, there are a number of criteria by which diagnostic images are evaluated and compared: spatial resolution, signal-to-noise ratio, and contrast-to-noise ratio.

Higher spatial resolution provides more detailed images for both functional and anatomical scans, as well as better localization of lesions or active areas of the brain during functional scans. For MRI, increased magnetic field strength offers increased spatial resolution. Figure 2 compares an axial slice of the brain imaged at (a) 1.5 Tesla. b) 7 Tesla and (c) a physical brain slice.

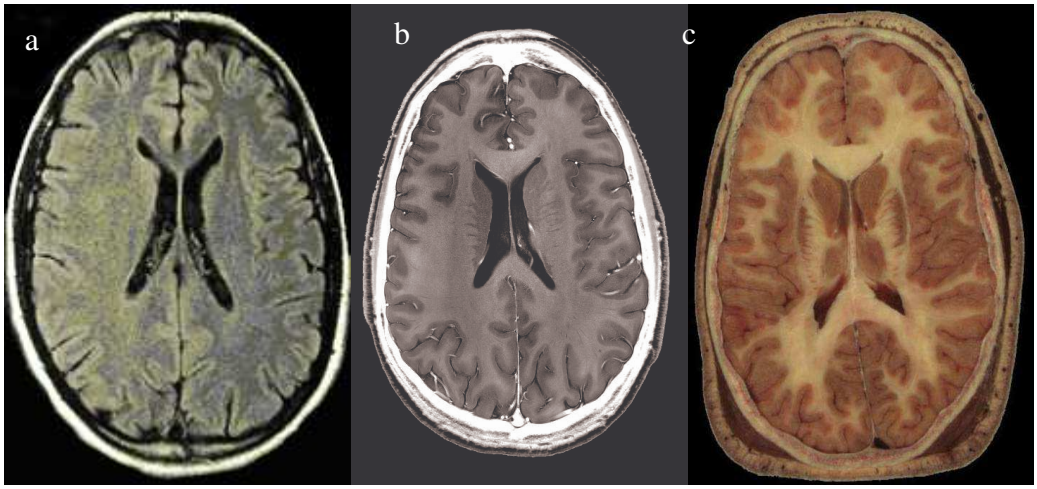

Figure 2. Spatial Resolution Comparison: (a) 1.5T (b) 7T (c) Physical Section.
Images: http://faculty.une.edu/com/fwillard/AxialMRI02/pages/MRI0346.htm; Roger Ordidge, University College London; www.berkeley.edu

Signal-to-noise ratio (SNR) is the ratio of the mean signal to the variation around the mean signal in space. SNR describes the quality of the signal used to create an image. In MRI, SNR is defined:

$$SNR \propto \frac{V \cdot N_p \cdot N_f}{\sqrt{bw} \cdot \sqrt{N_p \cdot N_f}} \tag{1}$$

Where V is voxel volume, the product $N_p * N_f$ is the number of measurements taken by the scanner, and bw is receiver bandwidth, which can be approximated:

$$\sqrt{bw} \propto \frac{N_p \cdot N_f}{T_{acq}} \tag{2}$$

Where T_{acq} represents the total acquisition time. The theoretical signal of an MR image is affected by Magnetic field strength, nuclear polarization, tissue relaxation times, slice thickness, voxel size and field of view. The signal actually measured in the receiver coil, however, depends on many other factors and is largely determined by noise sources including hardware instability, thermal noise, and physiology-related effects.

The contrast-to-noise ratio (CNR) is essentially the signal to noise difference between two tissues:

$$CNR_{AB} = SNR_A - SNR_B \tag{3}$$

CNR assesses the ability of a particular imaging technique to provide clinically useful contrast in the context of the amount of noise present. Together, the signal-to-noise and contrast-to-noise ratios describe the usefulness of a single image (Webb 2003).

For a series of images through time, Temporal SNR (tSNR) refers to temporal signal stability in individual pixels and is defined as the mean signal through time divided by the variance of that signal about the mean over the time course.

One significant development in MRI that critically depends on temporal signal stability is the ability to noninvasively map human brain functions. Functional magnetic resonance imaging (fMRI) measures interactions accompanying neurotransmitter release. When synapses fire, local oxygen demand increases; to meet this demand local blood flow increases significantly (Jezzard and Matthews 2001).

With an appropriate imaging sequence, MRI can be sensitive to these hemodynamic responses accompanying neuronal activity in the brain; such imaging techniques are termed Blood-Oxygen Level Dependent (BOLD) fMRI (Ogawa et al. 1990). However, since signal changes related to the BOLD effect are small (1-3% of the baseline signal) and the signal to noise ratio of the images is limited, many images must be acquired in both 'task' and 'control' conditions in order to detect areas of activity with statistical significance. Mean signal between task and rest conditions are often compared to some measure of noise (i.e. signal variance between images); thus, signal stability through time is critical to BOLD fMRI experiments.

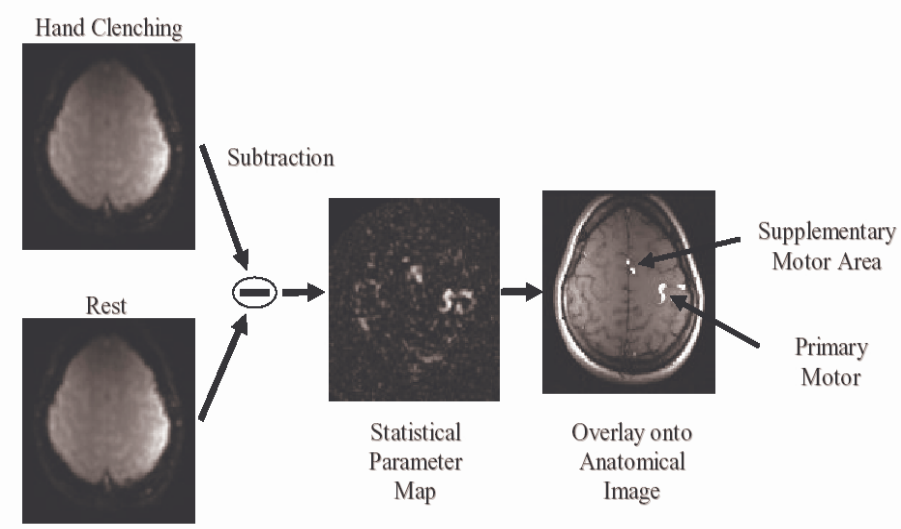

Figure 3. Generating a Functional Magnetic Resonance Image. Functional MR images are generated by subtracting images taken during activation from images during rest. The areas of differing signal intensity create a 'statistical parameter map,' which is overlaid onto an anatomical image to show which brain regions are activated. Image: Clare 1997.

In practice, the ability to detect functional activation is determined by the signal-to-noise ratio of individual images and temporal stability of the signal in a set of images through time.

Motivation & Context

fMRI analysis detects voxels whose signal time courses are well correlated with a task or test condition, but doing so reliably requires temporal signal stability. Many fMRI studies rely on fast, sensitive imaging techniques such as Echo Planar Imaging (EPI). This sensitivity is necessary to detect small signal changes due to neuronal activity; ideally only signal changes of this nature should be detected. In practice, however, many other sources of signal instability (thermal noise, hardware instability, subject motion and physiological noise (variation from intact tissues in living subjects)) affect image-to-image intensity fluctuations. This instability decreases statistical significance on functional activation maps, potentially causing activated areas to be overlooked.

While it is now common to correct for gross subject motion via spatial registration algorithms, few fMRI studies attempt to correct for physiological noise despite the fact that it constitutes a large fraction of the total noise and can be responsible for over 50% of image-to-image instability in functional experiments ((Weisskoff et al. 1993, Hu et al. 1995). Respiratory and cardiac processes are the most significant components of physiological noise, and here we focus on respiratory effects alone.

Several techniques for physiological noise removal have been suggested, including navigator echo, retrospective gating, digital filtering, k-space and image-space

based estimation, pulse sequence gating, and more (Hu et al 1995, Wowk et al 1997, Biswal et al 1996, Glover et al. 2000, Chuang et al. 2001, Le et al 1996).

The nature and magnitude of physiological noise effects can vary by individual, slice location, scan type and magnetic field strength, but they are always present when scanning living subjects. Characterizing noise sources which reduce temporal signal stability can lead to more sophisticated methods for their removal, improving the usefulness of fMRI data. Unfortunately, due to an incomplete understanding of the ways in which physiological processes affect the fMRI signal, no widely effective method for their correction has yet been developed.

A more robust technique for the estimation and correction of physiological effects, based on a clearer understanding of how those effects manifest in MR images, is needed. Ideally, methods for characterizing and correcting for these effects should be simple, retrospective, efficient, and widely applicable.

Organization of Thesis

Chapter II: A foundational review of the physics of MRI is presented, focusing in particular on signal formation, the effects of magnetic field inhomogeneity (susceptibility effects) and their implications for functional MRI.

Chapter III: A detailed review of the history of physiological noise characterization and correction in functional MRI is presented, followed by a discussion of parallel imaging and its relationship to SNR.

Chapter IV: Original research is presented and discussed, future work is proposed.

CHAPTER II

PRINCIPLES OF MAGNETIC RESONANCE IMAGING

Spin Physics

Magnetic resonance imaging is possible because of spin angular momentum (spin), an intrinsic property of subatomic particles determined by protons and neutrons. Atoms with an odd number of nucleons possess net spin angular momentum. These nucleons (spins) can be visualized as spinning, charged spheres that produce a small magnetic moment, making them subject to MR phenomena (Nishimura 1996).

Spin angular momentum is characterized by the quantum number *I*. Total spin angular momentum is $\vec{S} = \hbar\vec{I}$, where the magnitude of *I* is an intrinsic property of the nucleus, and $\hbar$ is Planck's constant[1]. The magnitude of spin angular momentum is:

$$|\mathbf{S}| = \hbar\sqrt{I(I+1)} \tag{4}$$

In a magnetic field applied along the *z*-axis, the possible values of the *z*-component of the angular momentum are

$$S_z = \hbar m_I \tag{5}$$

where $m_I = I, (I-1), (I-2), ..., -I$.

To exhibit NMR, the nucleus must have a non-zero value of *I*. The hydrogen nucleus is of special interest in medical imaging because of its single proton nucleus and high natural abundance.

[1] 1.055x 10^{-34} Joule-seconds

By $S_z = \hbar m_I$, the hydrogen nucleus may only have two possible values of S_z:

$$S_z = \pm\frac{1}{2}\hbar \tag{6}$$

A proton may be understood as an electrically charged, spinning gyroscope. This motion simulates a current loop about the axis on which it is spinning and produces its own magnetic field, similar to that of a bar magnet, which is subject to the effects of external magnetic fields. The strength of these interactions depends on the spin's 'magnetic dipole moment' $\vec{\mu}$, which is parallel to the spin axis and governs the behavior of the spin with external magnetic fields (Webb 2003). Specifically, interaction of the proton with an external magnetic field produces a torque, causing the spin to precess about the applied field B_0. *Precession* is circular motion of the axis of a spinning body (Nishimura 1996).

The magnetic moment $\vec{\mu}$ is related to spin angular momentum by the gyromagnetic ratio γ, a constant of proportionality specific to particular species of nuclei.

$$\vec{\mu} = \gamma\vec{S} \tag{7}$$

The energy of a magnetic moment in an externally applied magnetic field $\boldsymbol{B}$ is

$$E = -\vec{\mu}\cdot\vec{B} \tag{8}$$

Substituting for $\vec{\mu} = \gamma\vec{S}$ and $\vec{S} = \hbar\vec{I}$ we get:

$$E = -\hbar\gamma\vec{I}\cdot\vec{B} \tag{9}$$

Or, since by definition the magnetic field is applied parallel to the z-axis:

$$E = -\hbar\gamma I_z B_z, \qquad \text{or} \qquad E = -\hbar\gamma B_z m_I \tag{10}$$

For a proton with $m_I = \pm\frac{1}{2}$, there are two possible energy states: spin up (parallel to the external field; lower energy) and spin down (antiparallel to the external field; higher energy). A transition between the two states represents a change in energy:

$$\begin{aligned} \Delta E &= E(m_I = -\frac{1}{2}) - E(m_I = +\frac{1}{2}) \\ &= \frac{1}{2}\gamma\hbar B_0 - (-\frac{1}{2}\gamma\hbar B_0) \\ &= \gamma\hbar B_0 \\ &= \hbar\omega_0 \end{aligned} \tag{11}$$

Where

$$\omega_0 = \gamma B_0 \tag{12}$$

The equation $\omega_0 = \gamma B_0$ is known as the *Larmor Equation*, which governs precession of magnetization vectors and is central to magnetic resonance imaging. For an external field $\vec{B} = B_0\hat{z}$, ω_0 is the frequency of the photon that must be absorbed or emitted for a spin to make the transition between the two energy states. This is known as the *Larmor* frequency, which happens to be the same as the classical precession frequency of the proton magnetic moment (Haacke et al. 1999). For hydrogen, at a magnetic field strength of 1.0 Tesla, the Larmor frequency is 42.58 MHz, in the radiofrequency (RF) region (Nishimura 1996).

The Larmor frequency depends, for a given species of nuclei (constant γ), purely on the applied magnetic field. Imaging of human tissue makes use of the ability to manipulate large quantities of spins in water, fat and other organic molecules with a combination of external magnetic fields. The most intuitive way to do this is to treat a

given system as an ensemble of independent spins and observe their net behavior; that is, to focus on the *net magnetization* $\vec{M}$ of the spin ensemble.

In the absence of an external magnetic field, spins are randomly oriented due to thermal activity and the macroscopic net magnetization is zero. In the presence of an external magnetic field B_0, most spins assume opposite positions and cancel one another while a very small majority of spins will align with the externally applied field. This *net* magnetic moment along the direction of the applied field (the z- or longitudinal direction.) is what allows the magnetic resonance signal to be detected (Nishimura 1996).

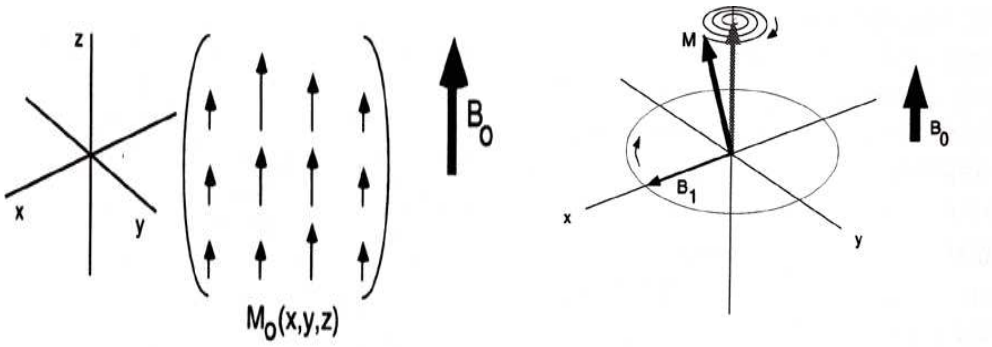

Figure 4. Spins Aligned With an External Magnetic Field. Image: Nishimura 1996.

Macroscopically, the B_0 field polarizes the system, inducing a net magnetization vector pointed in the z-direction of strength M_0. When aligned with the external field B_0, the nuclear spins exhibit resonance at the Larmor frequency, ω_0; that is, they will be 'excited' by a radiofrequency magnetic field tuned to the Larmor frequency and will oscillate to produce a signal based on the Larmor frequency as well. The spinning nuclei react to B_0 like a spinning top in a gravitational field, precessing about the field at a well-defined frequency (Nishimura 1996).

When placed in a magnetic field $\vec{B}$, the spin magnetization vector $\vec{M}$ will experience a torque. The equation of motion for $\vec{M}$ can be written:

$$\frac{d\vec{S}}{dt} = \vec{\mu} \times \vec{B}$$

$$\frac{d\vec{\mu}}{dt} = \vec{\mu} \times \gamma\vec{B} \qquad (\mu = \gamma\vec{S})$$

$$\frac{d\vec{M}}{dt} = \vec{M} \times \gamma\vec{B} \qquad (\vec{M} = \sum \vec{\mu}) \tag{13}$$

If $\vec{B}$ is time-independent and parallel to z such that $\vec{B} = B_0 \hat{z}$, then

$$\frac{d\vec{M}}{dt} = \vec{M} \times \gamma\vec{B} \tag{14}$$

Becomes:

$$\begin{aligned} &\frac{dM_x}{dt} = \gamma M_y B_0 \\ &\frac{dM_y}{dt} = -\gamma M_x B_0 \\ &\frac{dM_z}{dt} = 0 \end{aligned} \quad \text{With solutions:} \quad \begin{aligned} M_x(t) &= M_x(0)\cos(\omega_0 t) + M_y(0)\sin(\omega_0 t) \\ M_y(t) &= -M_x(0)\sin(\omega_0 t) + M_y(0)\cos(\omega_0 t) \\ M_z(t) &= M_z(0), \end{aligned} \tag{15}$$

where $\omega_0 = \gamma B_0$. (Clare 1997)

These equations describe the precession of the magnetization vector $\vec{M}$ about the z-axis. The angular frequency of the precession is identical to the Larmor frequency derived above.

Now consider, in addition to the static B_0 field applied along z, a time varying field B_1, applied perpendicularly to B_0 and oscillating at ω_0. Let B_1 be:

$$\vec{B}_1(t) = B_1(t)\cos(\omega_0 t)\hat{i} - B_1(t)\sin(\omega_0 t)\hat{j} \tag{16}$$

Plugging this into (14) yields:

$$\begin{aligned}
\frac{dM_x}{dt} &= \gamma[M_y B_0 + M_z B_1 \sin(\omega_0 t)] \\
\frac{dM_y}{dt} &= \gamma[M_z B_1 \cos(\omega_0 t) - M_x B_0] \\
\frac{dM_z}{dt} &= \gamma[-M_x B_1 \sin(\omega_0 t) - M_y B_1 \cos(\omega_0 t)].
\end{aligned} \tag{17}$$

If an initial condition $M(0) = M_0\hat{k}$ is defined, then the solutions for $\vec{M}$ are:

$$\begin{aligned}
M_x(t) &= M_0 \sin(\omega_1 t)\sin(\omega_0 t) \\
M_y(t) &= M_0 \sin(\omega_1 t)\cos(\omega_0 t) \\
M_z(t) &= M_0 \cos(\omega_1 t),
\end{aligned} \tag{18}$$

where $\omega_1 = \gamma B_1$. (Clare 1997)

This implies that by applying an oscillating magnetic field of frequency ω_0, the magnetization simultaneously precesses about B_0 at ω_0 and B_1 at ω_1.

Here we introduce a new frame of reference for viewing the evolution of the magnetization vector, the rotating frame, which rotates about the z-axis at frequency ω_0. If in the rotating frame an axis system (x', y', z) is defined, then (14) can be written:

$$\frac{d\vec{M}}{dt} = \gamma\vec{M} \times \vec{B}_{eff} \tag{19}$$

where $$\vec{B}_{eff} = (B_0 - \frac{\omega}{\gamma})\hat{k} + B_1\hat{i}' \tag{20}$$

Here, **(*i*', *j*', *k*)** are unit vectors in the (x', y', z) direction. The result of solving these equations is a magnetization vector which precesses about $\vec{B}_{eff}$, the *effective* magnetic field vector. If $B_0 = \frac{\omega}{\gamma}$, then $\vec{B}_{eff} = B_1\hat{i}'$, and $\vec{M}$ precesses about the x' axis.

Applying the $\vec{B}_1$ field rotates the magnetization vector about the *x*'-axis at an angular frequency $\omega_1 = \gamma B_1$.

The most common way to carry out an NMR experiment is to apply a short burst of resonant radiofrequency field $\vec{B}_1$, called an RF pulse, tuned to the Larmor frequency of the target spins. This applies a torque for time *t* which rotates the magnetization vectors by a 'tip angle' $\Theta = \gamma B_1 t$ creating a component of magnetization M_y in the *y*-direction. A tip angle of 90 degrees results in the maximum value of M_y. Once in the transverse plane, the magnetization precesses about the *z*-axis.

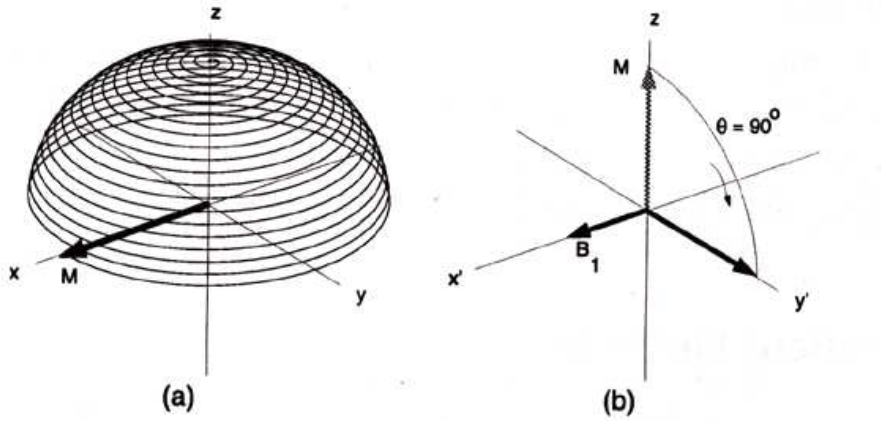

Figure 5. Precession About External Field B_0 in (a) Laboratory and (b) Rotating Reference Frames. B_0 is parallel to *z* and *z'*. In the rotating reference frame, the *z'* axis is identical to the stationary *z* axis in the laboratory frame, but the *x'* and *y'* axes rotate around the *z'* axis at the Larmor frequency. This eliminates the need to consider precession about the *z* axis in the vector model using the laboratory frame (Webb 2003). Images: Nishimura 1996.

MR Signal & Relaxation

Spins excited to the transverse plane will precess about the applied field, but because these spins are at a higher energy state they will also tend to transfer that energy to their surroundings to return to their equilibrium position, a process called relaxation.

Relaxation is characterized by three time constants, T_1, T_2 and T_2^*; these, coupled with proton density, form the MRI contrast mechanism.

Precessing protons lose energy to the surrounding lattice, causing the return of the magnetization vector along the z-axis (longitudinal axis). This effect, spin-lattice relaxation, is characterized by the time constant T_1. Different tissues have different inherent T_1; this difference is one basis for tissue contrast in MR imaging (Webb 2003).

Spins not only exchange energy with the surrounding lattice, but also among one another. This 'spin-spin relaxation' process is generally faster than spin-lattice relaxation and is characterized by T_2, the decay of magnetization in the transverse plane. The mechanism of T_2 relaxation involves loss of 'phase coherence,' which can be thought of as the maintenance of a constant phase relationship between the magnetic moments of the individual protons (Webb 2003).

The third relaxation parameter, T_2^*, incorporates the effects of 'pure' T_2 decay as well as the spatial variations in magnetic field in the body. T_2^* is defined as:

$$\frac{1}{T_2^*} = \frac{1}{T_2} + \frac{1}{T_2'} \tag{21}$$

Where T_2' describes decay due to magnetic field inhomogenieties of various origin, especially susceptibility effects which are pronounced at air/tissue and bone/tissue boundaries. In MRI, the value of T_2^* can be up to two orders of magnitude shorter than T_2 (Webb 2003). Since T_2^* is essentially a modified T_2 relaxation time, they are interchangeable depending on the level of accuracy desired or type of data available in a particular calculation.

The precession and relaxation of the net magnetization vector $\vec{M}$ is the source of the NMR signal, and its behavior is described by the Bloch Equation:

$$\frac{d\vec{M}}{dt} = \vec{M} \times \gamma\vec{B} - \frac{(M_x\hat{i} + M_y\hat{j})}{T_2} - \frac{M_z - M_0}{T_1}\hat{k} \tag{22}$$

where $\hat{i}, \hat{j}, \hat{k}$ are unit vectors in the *x*, *y*, *z* directions, respectively. M_0 is the equilibrium magnetization from the main field $\vec{B}_0$, and $\vec{B}$ includes the various applied magnetic fields. The Bloch equation can also be written by components, describing relaxation in the transverse plane (*x*-*y*) or along the longitudinal axis (*z*):

$$\begin{aligned}
\frac{dM_x}{dt} &= \gamma M_y(B_0 - \frac{\omega}{\gamma}) - \frac{M_x}{T_2} \\
\frac{dM_y}{dt} &= \gamma M_z B_1 - \gamma M_x(B_0 - \frac{\omega}{\gamma}) - \frac{M_y}{T_2} \\
\frac{dM_z}{dt} &= -\gamma M_y B_1 - \frac{(M_z - M_0)}{T_1}.
\end{aligned} \tag{23}$$

Immediately following an RF pulse, the magnetization vector has components:

$$\begin{aligned}
M_x(0) &= 0 \\
M_y(0) &= M_0 \sin(\Theta) \\
M_z(0) &= M_0 \cos(\Theta)
\end{aligned} \tag{24}$$

When plugged into the Bloch equations, this gives:

$$\begin{aligned}
M_x(t) &= M_0 \sin\Theta \sin(\omega_0 t) e^{-\frac{t}{T_2}} \\
M_y(t) &= M_0 \sin\Theta \cos(\omega_0 t) e^{\frac{-t}{T_2}} \\
M_z(t) &= M_0[1 - (-1\cos\Theta) e^{\frac{-t}{T_1}}]
\end{aligned} \tag{25}$$

Since the signal in MRI arises from precessing magnetization in the transverse plane of the, the signal in rotating frame can be represented as:

$$S' = \iiint M_{xy}'(x, y, z)dxdydz \tag{26}$$

Or, in terms of magnitude and phase:

$$S' = \iiint \rho_M(x, y, z) e^{i\phi(x,y,z)} dxdydz \tag{27}$$

where $\rho_M(x, y, z)$ is referred to as the proton density (Anderson and Gore 2004). The signal is detected according to its precessional frequency, and decays in a manner characterized by T_1, T_2 and T_2^*.

The goal of magnetic resonance *imaging* is to correlate spatial frequency measurements with spatial locations. If the applied field is simply the main static field B_0 in the z-direction, all the spins precess at the same resonance frequency $\omega_0 = \gamma B_0$ and, if excited, behave like oscillators inducing signals at the Larmor frequency. When the vast majority the protons in the sample are represented by just one chemical species such as water (as is the case with human imaging), the analysis described above simply gives the total signal from all spins regardless of their spatial location, as long as the applied field is uniform. Spatial localization is achieved by applying linear *gradient* magnetic fields in addition to B_0, which results in a spatially changing magnetic field across the sample.

The signal then varies spatially, with protons in the sample having varying frequency components according to:

$$\begin{aligned} \omega(x) &= \gamma B(x) \\ \omega(x) &= \gamma(B_0 + G_x x) \\ &= \omega_0 + \gamma G_x x \end{aligned} \tag{28}$$

Since the rotating frame is synchronized to the Larmor frequency, the precessional frequency in the rotating frame is:

$$\omega_x = \gamma G_x x \tag{29}$$

where x is the spatial coordinate along the field gradient, G_x is the gradient field strength at x, and B_x is the total magnetic field at x. The precessional frequencies for protons in the y- and z-directions are exactly analogous. Creative use of gradient fields allows one

to tune to the Larmor frequency of a group of spins at a particular spatial location, or slice, in an object. The application of a finite bandwidth RF pulse centered at the Larmor frequency of a particular slice of spins leads to the excitation of that slice, tipping the spins orthogonal to that gradient (Haacke et al. 1999).

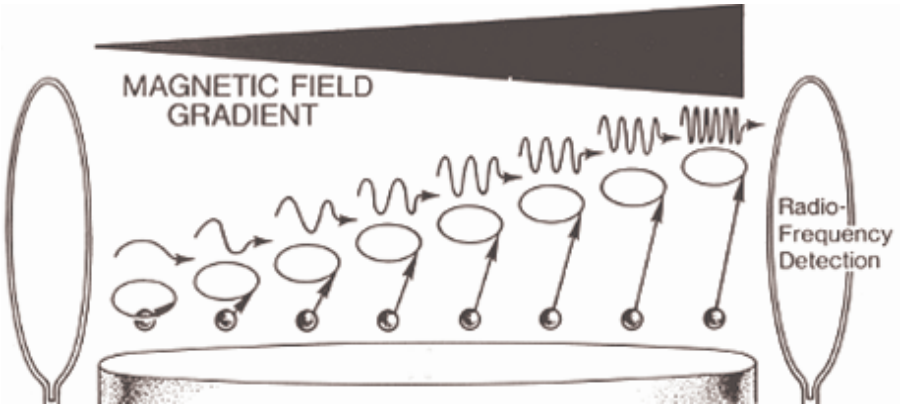

Figure 6. Gradient Fields Localize the NMR Signal. Magnetic gradient fields are imposed on top of the applied external field B_0 to introduce a spatially varying magnetic field strength. This changes the precession frequencies of spins at every point along the gradient, allowing for the localization of spins according to frequency. This is not unlike 'tuning in' to a radio station of a particular frequency. Image: St. Jude Children's Hospital.

In the context of imaging, the body can be visualized as an ensemble of tiny oscillating spins inducing RF signals. Purposefully creating an inhomogeneous field with gradients imparts spatial information to the resonant frequency of spins, and MRI maps this information in a way that allows retrieval of detailed anatomical and functional images (Nishimura 1996). Ideally, precession frequency would have a one-to-one correspondence with spatial position. In 2D imaging, the signal from spins in a given plane (slice) is encoded based on their frequencies (frequency encoding direction) and phases (phase encoding direction) relative to one another at a given time.

Figure 7. Planes of Magnetic Resonance Imaging. Sagittal, axial, and coronal images are generated based on the gradient used to select the slice for imaging. Sagittal corresponds to the *x*-, coronal to the *y*-, and axial to the *z*-gradient. Sagittal, axial images: St. Jude Children's Research Hospital.
Coronal image: http://medlib.med.utah.edu/WebPath/histhtml/neuranat/mrit1c21.html

Given this, and that spins relax to equilibrium over time, it is important, to design imaging pulse sequences that allow for maximum contrast in the area of interest. Here we focus on Single-shot, Gradient Echo, Echo Planar Imaging (EPI), an extremely fast MRI technique wherein a single excitation of the spin system is used to acquire the entire image, allowing sub-second imaging time. Because of this short acquisition time, contrast in EPI is dominated by T_2 and T_2^*. Therefore, the time taken to read a single line of the image must be much smaller than T_2^* so that many lines can be read before tissues relax to equilibrium. Thus, EPI necessitates strong gradient fields and rapid switching capabilities.

In Figure 8, we start at the bottom left corner of k-space and traverse an entire line of k_x (frequency encoding direction) before jumping up by one k_y (phase encoding direction) and returning across k_x. Rapidly switching gradients are used to bring spins back in phase to produce maximum possible signal within the T_2^* envelope at the time they are to be detected by the receiver coil.

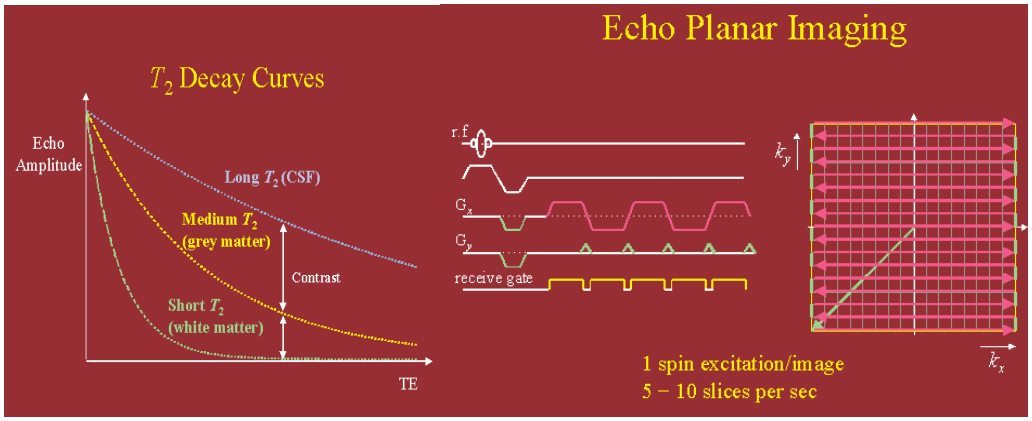

Figure 8. T2 Decay Curves and Simple Pulse Sequence for Echo Planer Imaging. The RF excitation pulse is followed by activation of a slice-selection gradient to localize spins for imaging. The slice selection gradient localizes the first of the three dimensions in imaging. Then the phase and frequency encoding gradients encode the remaining two spatial dimensions, those of the image itself, for later decoding. Image: http://www.fmrib.ox.ac.uk/~peterj/lectures/hbm_1/img044.GIF

Magnetic Susceptibility Effects

When spin phase depends only on physical position, (as in the case of a perfectly uniform main field with linearly varying gradient fields), we can find an expression for signal by in the rotating frame by integration:

$$S' = \iiint \rho_M(x, y, z) e^{i\phi'(x,y,z)} dxdydz \qquad (30)$$

Where $\phi'(x, y, z)$ refers to position-dependent phase accumulated in the rotating frame. If the time–evolution of spin phase is well-defined based on a uniform magnetic field, gradients can be employed to re-phase spins precisely for detection by the NMR receiver coil. In the presence of field inhomogeneities, however, spins precess with frequencies that no longer correspond to their spatial location, causing distortions such as shifts and warping in the reconstructed image. In the extreme case the signal is shifted outside the acquisition window and no image is obtained. In general effects of this nature are called 'off-resonance effects,' and most that manifest in this way are characterized by 'magnetic susceptibility.' Magnetic susceptibility is the extent to which an applied

magnetic field is distorted as it interacts with a material. Bulk susceptibility effects in an MR image occur when there are susceptibility variations across an image.

Rotating magnetization induces an electromotive force (EMF) in an RF receiver coil oriented to detect changes of magnetization in the *x-y* plane. The signal is measured when the receiver compares this coil voltage to the output of an electronic sine wave generator, called the local oscillator. If the local oscillator is set to the spin precession frequency $f_0 = \frac{\gamma B_0}{2\pi}$, then the result of the comparison is (30), the ideal signal, and is said to be *on-resonance* (Anderson and Gore, 2004).

If, on the other hand, the local oscillator is set to a frequency $f = f_0 + \delta f$, slightly different from that actually detected by the receiver coil, then the measured signal will not be the ideal case; instead it will precess relative to the ideal case (effectively, the rotating frame no longer precesses with spins at the Larmor frequency). Under this formulation, if $\delta f \neq 0$ the local oscillator is said to be *off-resonance*. Therefore, if $S'(t)$ is the ideal (i.e., on resonance) rotating frame signal, then

$$\tilde{S}'(t) = S'(t) \cdot e^{i 2\pi \delta f \cdot (t - t_0)} \tag{32}$$

is the measured signal when the local oscillator is off-resonance by δf, where t_0 is the time at which $\tilde{S}'(t)$ and $S'(t)$ have the same phase (Anderson and Gore, 2004).

Single shot imaging techniques like echo-planar imaging suffer more from off-resonance susceptibility effects, especially in the phase-encoding direction. In EPI, the read out gradient amplitude is generally much larger than the phase encoding amplitude. This is because the gradients must drive the spin system along a trajectory which traverses the sampled region of k-space many (e.g. 128) times in k_x, but only once in k_y.

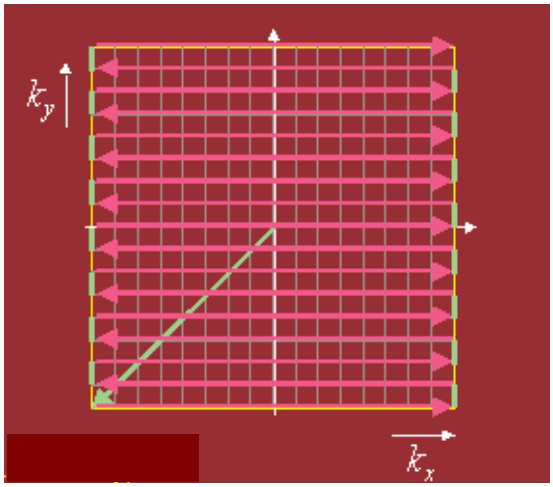

Figure 9. K-space sampling trajectory for Echo Planar Imaging. Each line of k_x is fully traversed before jumping to the next. Here k_x is the frequency encoding direction, while k_y is the phase encoding direction. Image: http://www.fmrib.ox.ac.uk/~peterj/lectures/hbm_1/img044.gif

The speed along the trajectory is therefore much larger in k_x than k_y (thinking in terms of the average speed in k_y). At a given value of k_y traveling in the k_x direction, neighboring samples are separated in time by the sampling interval τ_s. At a given value of k_x traveling in the k_y direction however, neighboring samples are separated by an interval which is $N^*\tau_s$, where N is the number of k_x sampling points (e.g. $128^*\tau_s$). Sampling frequency, or bandwidth, is defined as:

$$f_s = \frac{1}{\tau_s} \tag{33}$$

So for EPI, the effective sampling frequency in the phase encoding direction is:

$$f'_{sy} = \frac{1}{N\tau_s} = \frac{f_{sx}}{N} \tag{34}$$

where $f_{sx} = \tau^{-1}$ is the read out (and true) sampling frequency (Anderson and Gore 2004).

Phase errors have much longer to accumulate in the phase-encoding direction than in the frequency-encoding direction due to the relatively long time between samples in that direction.

For small frequency errors ($\delta f << f'_{sy}$) the phase error accumulated during each straight segment of the trajectory,

$$\delta\phi = 2\pi\delta f \cdot N\tau_s$$

$$\delta\phi << 2\pi N f'_{sy} \cdot \tau_s$$

$$\delta\phi << 2\pi_s \tag{35}$$

Are very small and can generally be ignored. However, the phase error accumulated along the entire trajectory, as k_y is driven from its minimum to its maximum value, may be significant (Anderson and Gore, 2004).

The following relation holds approximately for blipped echo-planar imaging if G_{PE} is interpreted as the time average of the phase encoding blips:

$$k_y(t') = \gamma G_{PE} t' \tag{36}$$

Where t' = 0 is defined as the point at which $\vec{k} = 0$, and G_{PE} is the amplitude of the (constant) phase encoding gradient. For convenience we assume that t_0 is the point at which the trajectory passes through $\vec{k} = 0$. Then $t-t_0=t'$ and we can rewrite (32) as

$$\tilde{S}'(k_y) = S'(k_y) \cdot e^{i\beta k_y} \tag{37}$$

Where

$$\beta = \frac{2\pi\delta f}{\gamma G_{PE}} \tag{38}$$

From our new expression for signal in the rotating frame, we can see that the optical transfer function (which describes how the signal is modified by off-resonance effects) for the phase encoding direction in EPI is

$$H(k_y) = e^{i\beta k_y} \tag{39}$$

The corresponding point spread function (the inverse Fourier Transform of the optical transfer function) is therefore:

$$h(y) = \frac{1}{2\pi} \cdot \int_{-\infty}^{\infty} e^{i\beta k_y} \cdot e^{ik_y y} dk_y$$

$$h(y) = \frac{1}{2\pi} \cdot \int_{-\infty}^{\infty} e^{i(y+\beta)k_y} dk_y \qquad (40)$$

$$h(y) = \delta(y + \beta)$$

Or, substituting for β

$$h(y) = \delta(y + \frac{2\pi\delta f}{\gamma G_{PE}}) \text{ (Anderson and Gore, 2004)} \qquad (41)$$

The image generated from measured k-space data is equal to the ideal image convolved (in the phase-encoding direction) with this point spread function.

Hence, a frequency error shifts image intensity in the phase encoding direction. Only the phase-encoding direction (here y) coordinates are affected because of the relatively low effective sampling frequency in this direction.

As an example, in a typical case where $\gamma G_{PE} = 2\pi \cdot 100$ Hz/cm, the image displacement is of $\frac{\delta f}{100}$ cm/Hz. Since frequency errors of tens Hertz are common and difficult to eliminate, displacements of a few millimeters are often encountered (Anderson and Gore, 2004).

If the frequency errors vary from pixel to pixel, severe image distortions that are difficult to correct can arise. Frequency errors of this nature are often caused by susceptibility effects, which are common in human imaging.

Most biological tissues consist of diamagnetic materials such as proteins, tissue, water or fat. Diamagnetic tissues have negligible magnetic susceptibility, while that of paramagnetic materials is significant. Hemoglobin, when saturated with oxygen, is diamagnetic. Deoxyhemoglobin, however, is paramagnetic and the difference in susceptibility between the paramagnetic sample and its diamagnetic surroundings causes field distortion, shortening the T_2^* relaxation time of local spins. Contrast develops between regions with varying ratios of oxy- to deoxyhemoglobin on T_2^* weighted images. Since oxyhemoglobin is transformed into deoxyhemoglobin by metabolic processes, this ratio can tell us something about how the body is functioning—this is the basis for BOLD fMRI.

Thus functional brain imaging depends on susceptibility effects on a molecular scale. Susceptibility effects on an image-scale, especially those due to physiological processes, are undesirable, difficult to correct, and are the subject of this work.

CHAPTER III

RELATED WORK

Physiological Noise

Weisskoff et al. (1993) made one of the first focused efforts to investigate the content of noise (signal changes not correlated with task) in functionally weighted MRI data. They investigated the time-course power spectrum in gray matter, white matter, and 'background,' and found noise in cortical regions to exhibit significant power at frequency components corresponding to physiological processes, namely the respiratory (~0.1-0.5 Hz) and cardiac cycles (0.8-1.2 Hz).

This foundational work exposed the presence of physiological noise processes in fMRI time course data, but did not explicitly attempt to characterize or correct them. It did, however, stimulate such work, and a number of approaches were quickly suggested in the literature.

Review of Physiological Noise Removal Techniques

Noll et al. (1994) used a navigator echo to measure and compensate for the phase error due to breathing. Navigator echo techniques reduce motion artifact signal fluctuations, but have difficulty with fMRI because inserting a navigator echo delays the data acquisition window, worsening T_2^* effects. In addition, navigator echo correction only reduces the phase-encoding artifacts in individual images and does not directly correct image-to-image variations.

Biswal et al. (1996) used digital filters to remove respiration-related noise. While digital filtering of the time series power spectrum works well in theory, in practice this method requires externally recorded physiological cycles to find the frequency bands to be filtered. Likewise, effectiveness of the filtering relies on the periodicity of the physiological motion and on the ability to acquire images fast enough to avoid spectral aliasing. Moreover, when the spectrum of functional activation overlaps with physiological fluctuation, this method cannot remove the artifacts without affecting the functional signal.

Hu et al. (1995) assumed physiological processes and the accompanying signal variations in MR data were pseudo-periodic, and then used externally monitored respiratory data to estimate physiological effects during an average 'unit cycle' of respiration. They modeled these effects with a 2nd order Fourier Series and subtracted them in k-space before image reconstruction. Using this method Hu et al. observed significant (20-60%) reduction of image-to-image signal variation in EPI images[2] and a 24% increase in number of pixels correlated with their functional visual task.

Because this technique was based on variations within a unit cycle (one full period of a physiological process), it was less sensitive to changes in the duration of each physiological cycle than previous methods. In addition, the technique was not sequence dependent and could be used under various experimental conditions (Hu et al. 1995). On the other hand, this method requires external monitoring of physiology and computationally intensive post-processing and off-line reconstruction of k-space data

[2] Gradient-echo EPI images acquired at 4T with TR = 0.3s, TE = 30m, matrix = 64x64, FOV = 20x20cm. 100-500 consecutive images.

which may not be readily available. Still, this method was successfully adapted and employed by Le et al. (1996) and Wowk et al. (1997).

In 2000, Glover et al. introduced RETROICOR (RETROspective Image-based CORrection technique), which was essentially Hu et al.'s technique modified to operate in image space; now fourier series estimate of unit cycle effects were fit to pixel time courses rather than k-space data. Glover et al. reduced physiological noise by an average of 40% compared to their implementation of the k-space method[3] (an average of 25%). In addition, RETROICOR was less computationally intensive than Hu et al.'s method because only magnitude images, as opposed to complex k-space data, are processed.

Image-based correction methods were further developed by Chuang et al. in 2001 with IMPACT (Image-based Physiological Artifacts estimation and Correction Technique) which, in theory, does not require external monitoring of physiological processes; instead, Chuang et al. estimate physiological frequencies from a histogram depicting the most commonly occurring frequency components in brain pixel time courses. Using IMPACT, significant reduction in respiration-induced signal variance, similar to that obtained with the k-space method, was observed in both simulated and real functional studies[4]. Both IMPACT and k-space corrections increased the activated area on functional maps by about 13%. Further, IMPACT demonstrated robust correction capabilities even at low respiratory frequencies or variable respiratory depths.

---

[3] Resting-state functional acquisitions used in a 2D spiral gradient-echo sequence at 3T with TR 250ms and 1000ms, TE = 30ms, FOV = 22x22cm, 3 slices, scan duration = 200s regardless of TR.

[4] Simulated and actual functional studies were acquired with single slice gradient echo EPI at 3T. TR = 250ms, TE = 40ms, 400 dynamic scans, matrix = 128x128 (simulation) or 64x64 (real), FOV = 25x25cm, slice thickness = 4mm. Visual stimulation was delivered by a pair of red light emitting diode goggles flashing at 8 Hz.

Removing the requirement for external physiological monitoring alleviates issues with simultaneous recording and retrospective synchronization and simplifies data acquisition. It also means that this method can easily be applied to previously acquired data for retrospective analysis. Further, because processing is done in image space, it can be utilized in institutions in which k-space data are not easily available.

One thing that all methods above have in common is the assumption of an additive model for physiological noise. That is, they assume the time series of intensities $y(t)$ in a pixel is corrupted by additive noise $y_\delta(t)$ such that the noise component $y_\delta(t)$ can be expressed as a Fourier series and subtracted from $y(t)$ to retrieve the 'true' measurement, or filtered out directly. Though these techniques achieved significant results under this assumption, work by Raj et al. (2000 & 2001) and Jezzard (1999) suggested that an additive model for physiological noise is incomplete.

Characterizing Respiration-Related Susceptibility Effects

Based on suggestions by Hu et al. (1995), Wowk et al. (1997) and later Jezzard (1999), that a major cause of respiratory noise is fluctuation of magnetic susceptibility—specifically that movement of organs in the chest and abdomen may be accompanied by susceptibility effects related to oscillation of the magnetic field in the brain—Raj et al. (2000) set out to quantify the effects of variations in the size and magnetic susceptibility of the air cavity in the lungs.

They developed a theoretical model based on the following principle: when a human body is placed in a uniform magnetic field B_0, its diamagnetism results in a slight decrease in the effective field in tissue, while paramagnetic air cavities (i.e. those

containing molecular oxygen such as the lungs) within the body tend to increase the effective field in their neighborhood (Raj et al 2000).

Using this model they acquired simulated and real images[5] in the presence of a spherical cavity using variable different susceptibility values for the cavity gas (phantom oxygen concentration varied from 0-100% oxygen). They observed image shifts and distortions occurring as a function of distance from and susceptibility of the cavity (larger concentrations and smaller distances resulted in larger distortions). This was quantified with measurements of the motion of the image's center of mass, and was consistent with their theoretical model.

They concluded that variation within the chest cavity during respiration, both in lung volume and oxygenation may produce significant susceptibility-related effects in EPI images. More specifically, a spatially invariant field shift in the imaging plane leads to a simple shift of the image, whereas a spatially varying field leads to inhomogeneity-based shifting of image intensity. In particular, in axial echo-planar images, the artifact manifests as an approximately linear distortion of the image profile and a shift of the image in the phase-encoding direction (Raj et al. 2000).

The following year, Raj et al. (2001) quantified the nature of noise due to respiration in the context of EPI fMRI[6] and demonstrated specific susceptibility-related artifacts in brain images. In two studies, they imaged the brain of a subject with a water phantom doped with 10mM copper sulfate placed near the head. They observed a ~1%

[5] Spin Echo EPI experiments performed on a water and gas phantom at 1.5T with TR = 4s, TE = 80ms, matrix = 64x128, FOV = 20x40cm, 8 slices, 1mm thickness, 2cm gap.

[6] Gradient-echo EPI acquired at 1.5T with TR = 400ms, TE = 60ms, slice thickness = 10 mm, no gap, resolution 3.12x3.12mm (most) or 4.68x4.68 (copper sulfate) acquisitions, matrix 64x64, four runs of AP phase encoding, four runs of LR.

signal variation at the respiratory frequency in the phantom, decreasing further from the chest. This indicated that susceptibility changes in the chest were responsible the observed signal change.

They also observed a shading of image intensity in the phase encoding direction due to spatially variant magnetic field errors, and a shift of the entire image in the phase encoding direction due to spatially constant field errors. In addition, they saw global signal decrease due to intravoxel dephasing.

In order to conclusively show that these artifacts were due to susceptibility effects and not simply gross head motion, the experiments were repeated with the phase encoding gradient switched. The shading and movement were observed in phase encoding direction of the subject, clearly indicating susceptibility-related origin (Raj et al. 2000).

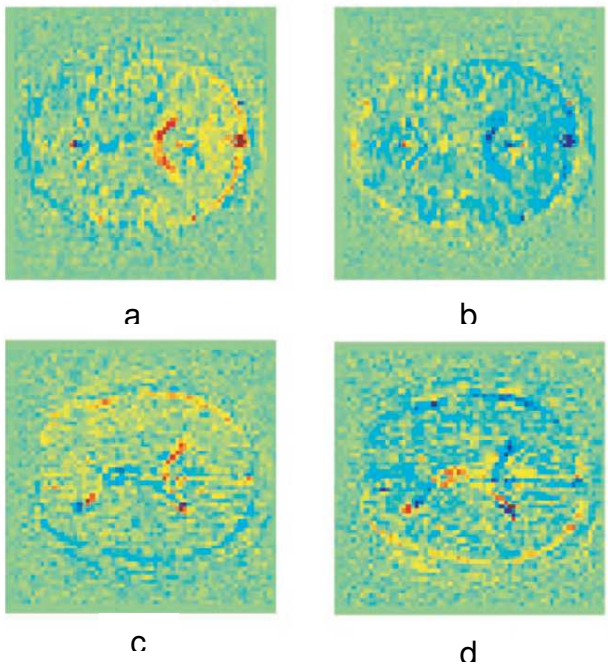

Figure 10. Susceptibility-related image shifting and shading. Raj et al. observed an intensity shading effect on the order of 1% in the phase encoding direction when comparing images at respiratory extrema to the 'mean' image through time. (Raj et al.. 2001).

Likewise, the center of mass of the image shifts in the phase encoding direction, and the coordinate of the center of mass associated with the phase encoding direction exhibited significant power at the respiratory frequency. Together, these data clearly demonstrate that susceptibility changes due to respiration cause artifacts in brain images.

This does not necessarily mean that respiration does not cause motion artifacts, but it does mean that, in addition to any motion artifacts, respiratory processes cause susceptibility-related artifacts in echo-planar images.

Based on this, Raj et al. suggested that respiration effects may not be well characterized as additive noise and that an alternative model based on physical origins of susceptibility variations may be more appropriate.

We have reviewed a number of methods for correcting physiological noise in MR images, but we have also shown that the additive model for physiological noise that these methods assume may be incomplete.

Beyond knowing how susceptibility effects manifest in MR images, it is also important to know if a chosen acquisition scheme introduces any artifacts of its own into the images. If so, the nature of any such effects, and their interactions physiological effects, if any, must be accounted for to insure correction accuracy.

The limitations of Echo-Planar Imaging in this regard are well-documented; as discussed above, the relatively long time between steps in the phase-encoding direction makes the technique especially sensitive to susceptibility effects and B-field inhomogeneities. New techniques have recently been developed which allow faster k-space coverage but may introduce their own artifacts into the images they create.

Parallel Imaging: Sensitivity Encoding (SENSE)

Parallel imaging is a powerful new way of acquiring MR data that significantly reduces k-space coverage time. Sensitivity Encoding (SENSE), a popular parallel imaging technique, is based on the idea that receiver coil sensitivity implies information about the origin of detected MR signals (Pruessmann et al., 1999). Thus, parallel acquisition techniques employ arrays of receiver coils to sample distinct information in k-space simultaneously and reconstruct undersampled data using spatially varying coil sensitivity profiles.

In combination with single-shot methods, parallel imaging can increase the matrix size without changing the readout period or shorten acquisition time by reducing echo train length. However, compared with full Fourier encoding, parallel imaging incurs a signal-to-noise ratio penalty due to lower sampling density and exhibits spatially varying noise amplification depending on coil sensitivity (Pruessmann et al. 1999).

There are two kinds of noise in SENSE images: noise in sampled values and noise in sensitivity data. Unlike with conventional single-coil Fourier imaging in which noise is independent of pixel value, noise may be correlated between parallel receiver channels. This introduces artificial correlation between simultaneous samples, resulting in image artifacts familiar from single-coil imaging occurring periodically with varying intensity across the field of view.

For similar reasons noise in SENSE images does not have the common square-root dependence on the number of samples taken. With SENSE, SNR is characterized by the square root of the number of samples acquired and specific physical conditions such as coil sensitivity and arrangement when the data is acquired (commonly described by the

geometry factor, *g*). Generally speaking, *g*-factors increase with increasing undersampling rate (R) and decrease as more receiver channels are used. An optimal coil set-up is characterized by trade-offs among absolute sensitivity, individual channel noise, coil coupling, and coil geometry.

SENSE reconstructions are also subject to systematic errors (due to tissue motion, main field inhomogeneity, eddy currents, gradient non-linearity), typically manifesting as regional over- or under-estimation of signal depending on coil sensitivity. This can interfere with reliably detecting functional MRI activations (Pruessmann et al. 1999).

For serial imaging, the induction signal detected in the receiver coil is proportional to the voxel volume V, and number of samples ($N_p * N_f$), while the noise scales with the square root of the number of samples, and with the acquisition bandwidth of the receiver (*bw*).

$$SNR \propto \frac{V \cdot N_p \cdot N_f}{\sqrt{bw} \cdot \sqrt{N_p \cdot N_f}} \tag{42}$$

The application of sensitivity encoding introduces spatially varying noise described by the geometry factor, g (Schmidt et al. 2005):

$$\begin{aligned} SNR &\propto \frac{V \cdot \sqrt{T_{acq}}}{g} \\ &\propto \frac{V}{g \cdot \sqrt{R}} \end{aligned} \tag{43}$$

Where T_{acq} is acquisition time and R is SENSE reduction factor. According to (43), for an optimal coil geometry (g = 1) the SNR should drop from 100% at R = 1 to 71% at R = 2 and 58% at R = 3. However, the $\frac{1}{g \cdot \sqrt{R}}$ dependency holds strictly for

thermal noise only. In human subjects image noise is additionally influenced by fluctuations due to pulsatile blood flow, respiration, subject motion and, in particular, physiological noise.

The effect of this SENSE-related SNR loss on the sensitivity in BOLD fMRI is not directly evident because of the added contribution of susceptibility-related physiological effects. BOLD fMRI sensitivity scales with stability of the image intensity time course, which is determined by a combination of intrinsic image SNR and physiological noise. In functional MRI, the most important factor is the ability to detect brain activation at high levels of statistical significance, and this requires signal stability through time. Thus, the interactions of SENSE and fMRI detectability are of interest.

SENSE and Functional MRI

De Zwart et al. 2002, studied the effects of SENSE-EPI-fMRI and conventional EPI-fMRI in a finger tapping experiment. Their results, indicating an average increase in temporal variance of 34% accompanied by an 18% reduction in t-score, suggested that SNR penalty incurred with SENSE does not necessarily lead to an equal loss in fMRI sensitivity, depending on relative contributions of thermal and physiological noise (De Zwart et al., 2002).

The following year, Preibisch et al. (2003) examined motor task functional activation and found SENSE with R = 2 substantially reduced distortions and blurring, while signal-to-noise and statistical power (measured by cluster size and maximum t value per unit time) were reduced less than expected. In fact, the time course SNR at matrix size 192 is almost twice as high as expected from theory; they suggested this was

due to a reduced contribution of physiological noise. At R = 3, however, the additional gain in speed and distortion reduction was quite small, while signal-to-noise and statistical power dropped significantly.

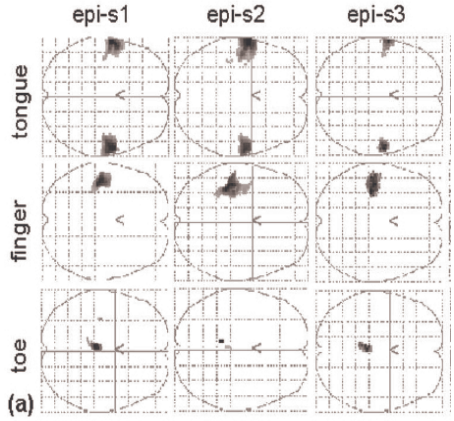

Figure 11. Functional activations at different SENSE reduction factors. Functional activations detected by Preibisch et al at with R =1 (known on Philips scanners as CLEAR), R = 2 and R = 3. Statistical significance did not decrease as much as theory would predict at R = 2; the losses at R = 3 were significant. Image: Preibisch et al. 1999.

In 2005, Schmidt et al. used SENSE-fMRI to investigate the medial temporal lobe (including the hippocampus and parahippocampal gyrus). This area is generally associated with higher cognitive functions and, due to its central location in the brain, tends to be more sensitive to susceptibility effects. Moreover, because high-order cognitive functions are more difficult to test with fMRI, BOLD signal changes in this region tend to be ~1% as opposed to the 2-3% often found in primary sensory or motor cortices, making temporal signal stability particularly important (Cohen and Bookheimer, 1994). They demonstrated steady SNR decreases with increasing R. As with previous studies, however, the SNR did not decrease as quickly as theory would predict.

Schmidt et al. (2005) argue both reduced T_2^* effects and a changed contribution from physiological noise may account for the higher SNR ratios than what is expected.

However, because physiological effects are susceptibility-related, and susceptibility effects scale with field, Schmidt et al. note that physiological noise may exceed intrinsic noise at higher field strengths.

Overall, these studies agree that application of SENSE-EPI with reduction factors of $R \leq 2$ improved fMRI results. At R = 2, distortions and blurring were substantially reduced while, possibly due to a signal strength dependency of physiological noise (Krueger and Glover, 2001; Krueger et al., 2001), the time-course signal-to-noise and statistical power were hardly affected. As above, the additional gain in speed was marginal at R = 3 while time-course signal-to-noise and statistical power clearly declined.

Thus, sensitivity encoding permits considerable scan-time reduction with respect to standard Fourier imaging. In terms of practical value the most relevant characteristic of the technique is flexibility, and the most critical issue is SNR. Hence the method is appropriate only when the need for scan speed or higher scan resolution in the same amount of time outweighs SNR concerns; this tradeoff is of particular concern in fMRI, where temporal signal stability is key. These studies argue that the resilience of SNR in SENSE images is due to contributions of physiological noise, but none have quantified the nature of the interactions between physiological noise and parallel imaging. This a primary goal of the research presented here.

CHAPTER IV

SENSE & SUSCEPTIBIILTY

Introduction

Functional MRI provides insight into the human brain, but is critically dependent on the time-stability of the MRI signal. One of the largest contributors to temporal signal instability is noise of physiological origin, but understanding of how these effects manifest in MR images is incomplete. Here we attempt to synthesize and evolve previous work, examining the effects of both physiological noise and SENSE, separately and together, on the time course of magnetic resonance images. We do so with the aim of better developing more effective correction techniques for SENSE- and physiology-related noise artifacts, in order that the utility of fMRI data might be increased.

Project Hypothesis

Given that a significant portion of physiological noise artifacts are due to susceptibility effects, and in light of the suggestion that relative contributions of respiratory noise are responsible for experimentally observed temporal SNR at increasing SENSE factors, we suggest the following:

The sensitivity of BOLD fMRI scales with stability of the image time course, which is determined by a combination of intrinsic image SNR and physiological noise levels. The use of SENSE will reduce intrinsic image SNR (by g and R-dependent noise amplification), but because physiological processes are independent of acquisition method, their absolute contributions to the images should not change appreciably with

SENSE. Thus, the SNR penalty for applying SENSE in fMRI should depend on the relative contribution of intrinsic image noise to the total temporal variance.

In cases in which temporal stability is fully determined by intrinsic noise (e.g. thermal noise sources as in a phantom), fMRI sensitivity penalty of approximately *g*sqrt(R)* is expected. On the other hand, when physiology-related instabilities prevail, the penalty incurred with SENSE is expected be less than *g*sqrt(R).*

Thus, if respiratory noise is a significant source of temporal variation in image data, and SENSE shortens the acquisition window, increasing SENSE factors will be characterized by smaller losses in temporal SNR than predicted by *g*sqrt(R),* accompanied by less severe T_2^*-related susceptibility effects. As SENSE increases, intrinsic image SNR decreases, and temporal signal stability becomes image-SNR limited rather than physiological noise-limited; at very high SENSE factors, therefore, we expect the SNR loss to approach the theoretical value of *g*sqrt(R).*

In addition, if respiration-related B_0 inhomogeneities degrade temporal SNR by increasing image-to-image variance, temporal SNR should be higher during periods of breath-hold. Likewise, respiratory artifacts should decrease as distance from the chest increases in both SENSE and conventional acquisitions.

Since functional MR activation maps are calculated from image data, ideally we desire a generally applicable technique would be available to characterize and correct for the physiological noise based image data. Concerning image data, we propose the following:

Since respiratory effects cause image shift and intensity shading, the motion of the image set's center of mass through time should be correlated with respiration in the

phase encoding direction. Based on this, it should be possible to estimate the respiratory waveform based on the motion of the center of mass alone. Estimating the motion of the center of mass depend on signal stability both spatially and in time. And because respiratory effects are expected to be dominated by intrinsic noise at higher SENSE factors, and the SNR loss incurred by SENSE images is most severe in the image center where sensitivity maps are less reliable, we expect using the center of mass in this way will become more difficult as SENSE increases.

Conversely, because IMPACT uses power spectra to estimate respiratory effects, and because we do not expect the absolute contribution of physiological noise to change a significantly SENSE increases, IMPACT should be relatively unaffected by increasing SENSE. We investigate these effects, and others, below.

Data Acquisition

Eight healthy volunteers were scanned on the VUIIS 3 Tesla Philips Scanner. All subjects were treated in accordance with IRB standards. For each subject, physiological processes were monitored with a pneumatic belt around the abdomen and a pulse oximeter on the right index finger. Echo planar images were acquired as follows: 80x80 matrix reconstructed to 128x128; TR = 400ms; TE = 35ms; 400 dynamic scans; 3 slices; 5 mm thickness; 5 mm slice gap; FOV = 220 mm^2.

When possible, image sets were acquired for both normal breathing and then prompted breath-hold conditions, with phase encoding direction first in the anterior-posterior (AP), and then left-right (LR) directions; each combination was collected with No Sense, CLEAR, SENSE R =2 and SENSE R = 3, for 16 possible protocols per subject.

For each subject, 12 to 16 data sets were acquired in groups of 4. On 4 of the 8 subjects, the normal breathing phase encode LR acquisition was omitted due to time constraints.

All studies were acquired with the Philip's Scanner Dynamic Stabilization feature deactivated. This feature compensates for frequency drift (and thus image drift), by recalculating the main-field larmor frequency (f_0) every TR. Because physiology-based susceptibility effects are frequency-related, it is possible that susceptibility-related image shift could be 'accidentally corrected' by Dynamic Stabilization. Thus, this feature was disabled to prevent interference with the effects we wished to observe.

All analysis was performed in Matlab 7 on a Dell Inspiron 6000 Laptop running custom-written code. Data were then compiled and compared quantitatively in Microsoft Excel.

Results & Discussion

There were five specific aims of this study:

1) To determine the contribution of respiratory power to tSNR;

2) To determine the effect of distance from chest cavity on respiratory power and tSNR;

3) To validate the effects of switching the phase encoding gradient on susceptibility-related effects;

4) To evaluate correlations between motion of an image set's center of mass through time with physiological measurements.

5) To evaluate correlations between the respiratory time course estimated from image data and physiological measurements of respiration.

The findings of investigating these five effects can be summarized in two related but distinct sections: 1) Contributions of respiratory power to temporal signal stability and 2) Motion of center of mass as a respiratory estimator. These are discussed in detail, comparing three parallel imaging conditions (CLEAR, R=2, R=3) under normal breathing and breath holding conditions, followed by a comprehensive summary.

Contributions of Respiratory Power to Temporal Signal Stability

A number of studies discussed above have demonstrated significant noise components at physiological frequencies in fMRI studies, but none have evaluated the precise relationship between the power of physiological frequencies and temporal signal stability. Here we quantify the contributions of respiratory power to tSNR during normal breathing and breath holding under different parallel imaging conditions.

Specific Methodology

For each data set, pixels outside the brain were masked to eliminate ghost artifacts, and the time course for pixels inside the brain were detrended and normalized. Image data were retrospectively synchronized with externally monitored physiological data and, if the study involved breath holding, normal breathing vs. breath hold blocks were manually differentiated. A temporal mean image was then calculated (mean signal over time for each pixel) and temporal signal to noise (tSNR) maps (mean value / standard deviation of each pixel's time course) were generated and spatially filtered with a Gaussian kernel (3x3, st. dev. = 0.5). Pixel magnitudes on these maps were summed as a measure of signal stability through time.

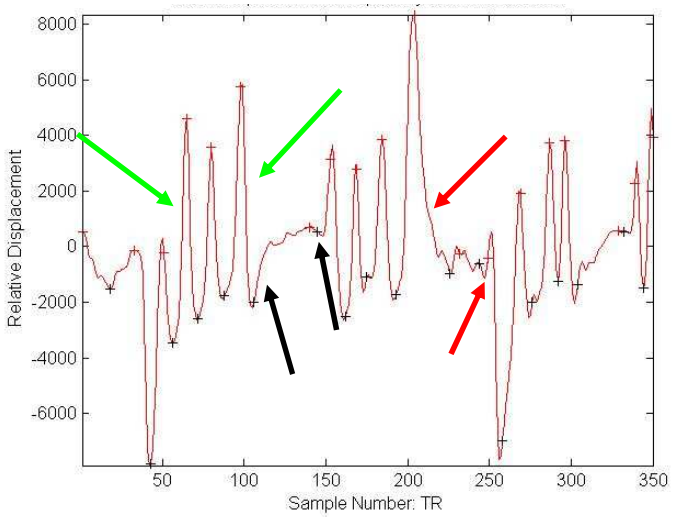

Figure 12. Representative monitored physiology for a breath hold study. Subjects were instructed to engage in two types of breath holds: hold at full exhale and hold at full inhale. These were characterized in different ways. Black Arrows: exhale breath-hold; Red: inhale breath-hold; Green: normal breathing.

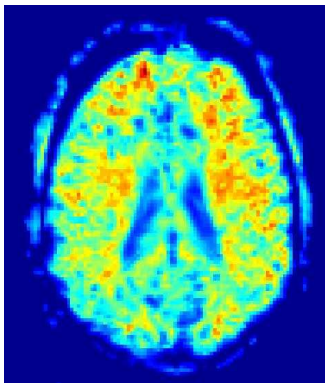

Figure 13. tSNR map for an AP normal breathing acquisition without SENSE.

For breath-hold studies, tSNR maps were generated for individual normal breathing and breath-hold blocks instead of for the entire time course. Temporal power spectra were then calculated for every pixel in the brain and a mean power spectrum for the image data was obtained by averaging these. A temporal power spectrum was acquired for each externally monitored physiological data set as well, which was filtered (Gaussian 1x450, st. dev. = 250) and downsampled (from 500 Hz to Once per TR) prior to spectral estimation.

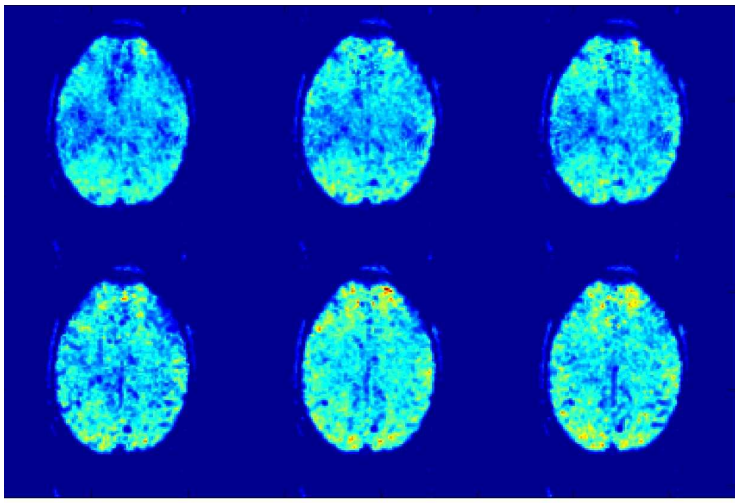

Figure 14. tSNR maps generated from an AP phase encode breath-hold acquisition without SENSE. Top images are tSNR images during normal breathing blocks; bottom images are those generated during breath hold blocks.

From the power spectrum of externally monitored respiration, a peak respiratory frequency was determined, and a respiratory range (peak +/- 0.03 Hz) was defined. Then, the fractional contribution of respiratory power to the total variation of each pixel in the brain was calculated as the power within the respiratory range relative to total spectral power.

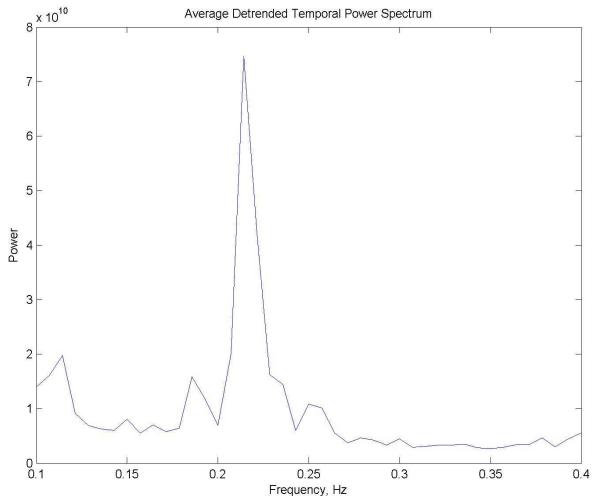

Figure 15. Mean power spectrum for an AP acquisition without SENSE.

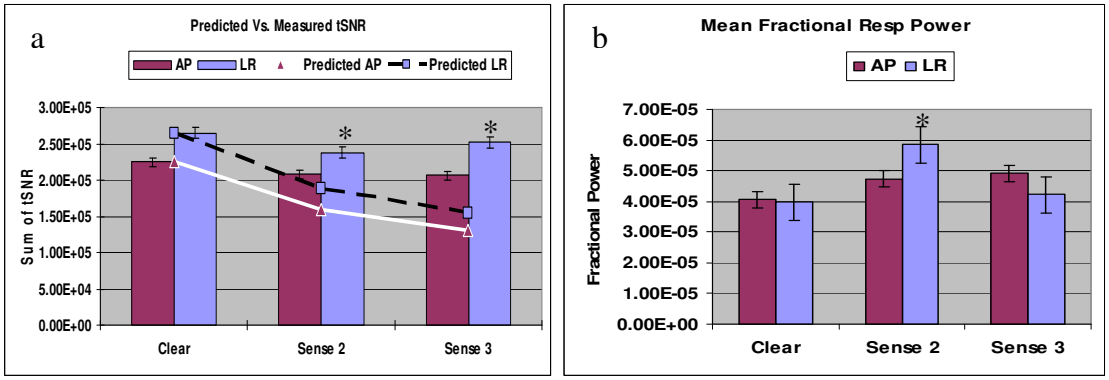

Figure 16. (a) Predicted vs. measured temporal signal to noise as a function of SENSE. (b) Mean fractional respiratory power as a function of SENSE. Asterisks denote significant difference from CLEAR condition ($p < 0.05$)

Comparing fractional respiratory power to predicted (dotted) and to measured (solid) temporal SNR, a number of trends emerge. First, tSNR decreases more slowly than theory predicts for thermal noise alone—mean tSNR is 30.4 % (AP) and 26.5% (LR) larger at R = 2 and 58.17% (AP) and 64.2% (LR) larger at R = 3 than theoretical prediction relative to CLEAR.

Second, tSNR is significantly higher (mean 16%) in all three conditions for LR phase encoding than for AP regardless of SENSE factor.

Third, temporal SNR tends to decrease and mean fractional respiratory power tends to increase as SENSE reduction factor increases. There is a clear relationship between the two, best demonstrated by the AP (red) acquisitions:

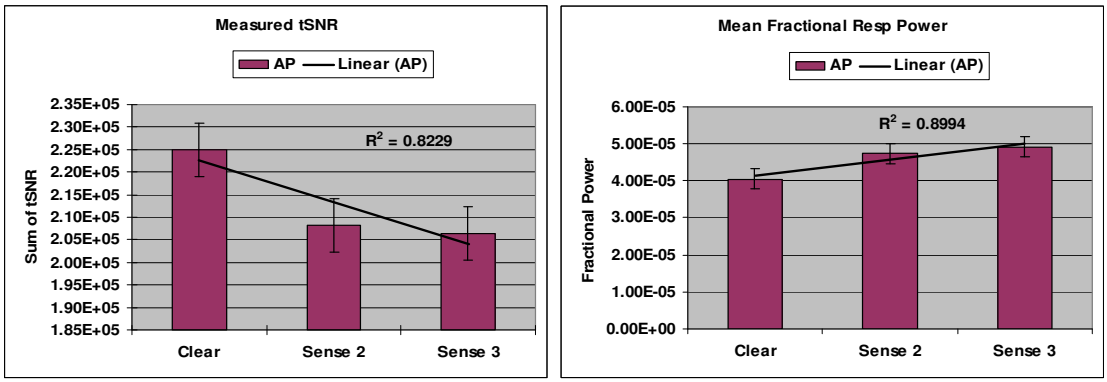

Figure 17. Mean tSNR decreases linearly while Mean Fractional Respiratory power for AP acquisitions increases linearly as SENSE reduction factor increases.

Fitting a line to mean fractional respiratory power yields $R^2 = 0.8994$; fitting to tSNR yields $R^2 = 0.8229$. The LR (blue) acquisitions do not follow a linear trend; fractional respiratory power jumps significantly at R=2, preventing a linear fit, but the tSNR value at R = 2 also drops significantly, showing that the two are related.

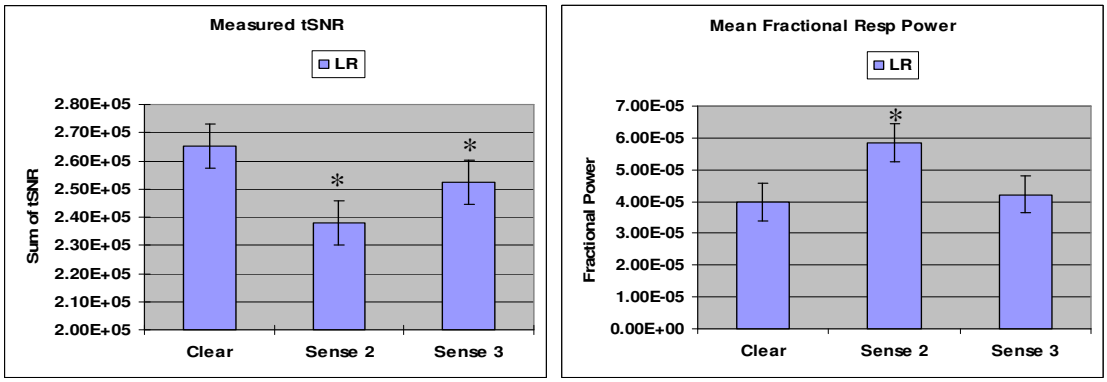

Figure 18. Mean tSNR and Mean Fractional Respiratory power for LR acquisitions did not behave linearly SENSE reduction factor increases due to unusual behavior at R = 2. Asterisk denotes significant difference from CLEAR condition ($p < 0.05$).

Breath hold data show similar changes in measured vs. predicted tSNR. Mean tSNR is 29.1% (AP) and 31.8% (LR) larger at R = 2, and 36.0% (AP) and 44.7% (LR) larger at R = 3 than theoretical predictions relative to CLEAR.

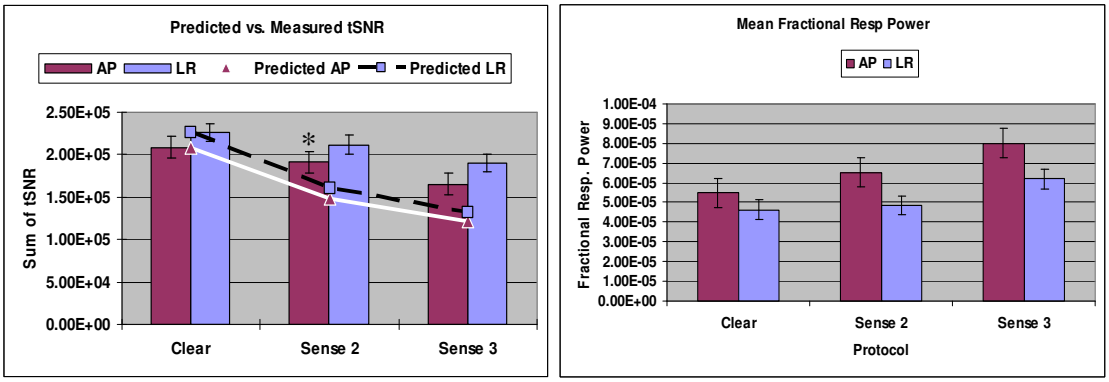

Figure 19. (a) Mean fractional respiratory power as a function of SENSE for a Breath Hold acquisition. (b) Predicted vs. measured temporal signal to noise as a function of SENSE. tSNR decreases with increasing SENSE (and increasing fractional respiratory power), but more slowly than theory predicts. Asterisks indicate significant difference from CLEAR ($p < 0.05$).

Again acquisitions with LR phase encoding exhibited an average of 11% greater tSNR, regardless of SENSE factor, than those acquired with AP phase encoding. These were accompanied by significantly (22%) lower fractional respiratory power values compared to their AP counterparts.

Here both AP and LR show linear increases in fractional respiratory power (R^2 = 0.99 (AP); R^2 = 0.85 (LR)) and decrease in tSNR (R^2 = 0.99 (AP); R^2 = 0.99 (LR)) as SENSE increases.

In general, fractional respiratory power magnitudes for the breath hold acquisitions were increased by ~ 30% compared to the normal breathing acquisitions. These are accompanied by significant decreases of 17% in tSNR over the full time course of breath-hold acquisitions.

Breaking breath-hold acquisitions into periods of normal breathing and periods of breath-hold supports this linear trend: mean tSNR for both normal breathing and breath hold blocks in both AP and LR acquisitions decreases linearly ($R^2 > 0.95$ for all four series). Here all values of tSNR are significantly different from one another ($p < 0.05$) except CLEAR normal breathing vs. CLEAR breath hold for both AP and LR conditions.

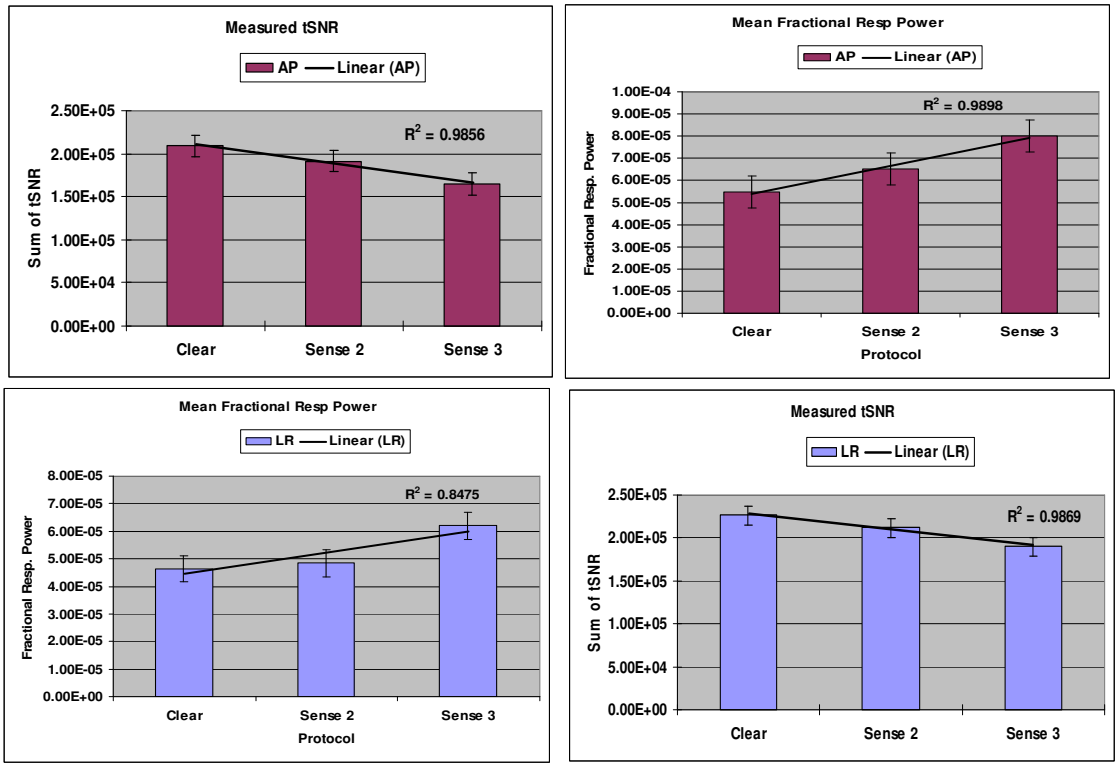

Figure 20. Mean Fractional Respiratory power for both AP and LR acquisitions increases in a linear fashion as SENSE reduction factor increases in the breath-hold studies.

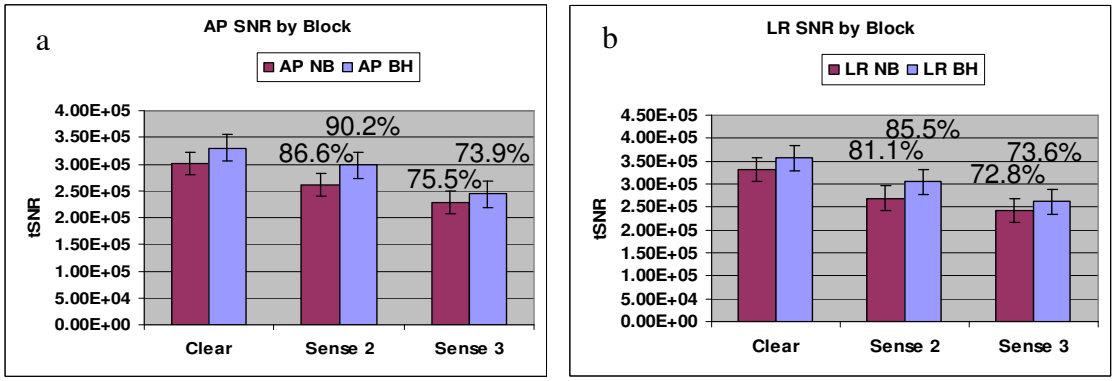

Figure 21. a) tSNR by block for an AP breath-hold acquisition. b) tSNR by block for an LR breath-hold acquisition. tSNR decreases with increasing R, and breath holding blocks consistently demonstrate higher tSNR than normal breathing blocks. Percentages are relative to CLEAR.

tSNR is higher (7%) for LR acquisitions, as above, under both normal breathing and breath-holding conditions. Further, mean tSNR for breath hold (blue) is on average 9% larger than for normal breathing (red) for both AP and LR acquisitions.

Power spectra for breath-holding studies reveal wider, lower amplitude distribution of power in the respiratory range (0.1-0.4 Hz) with no well-defined 'respiratory frequency;' instead, though amplitudes are generally lower, there is more integrated power (total variance) over the entire range of frequencies. Fractional respiratory powers *of the entire respiratory range* of the *entire time course* for breath hold studies average 30% larger than normal breathing acquisitions.

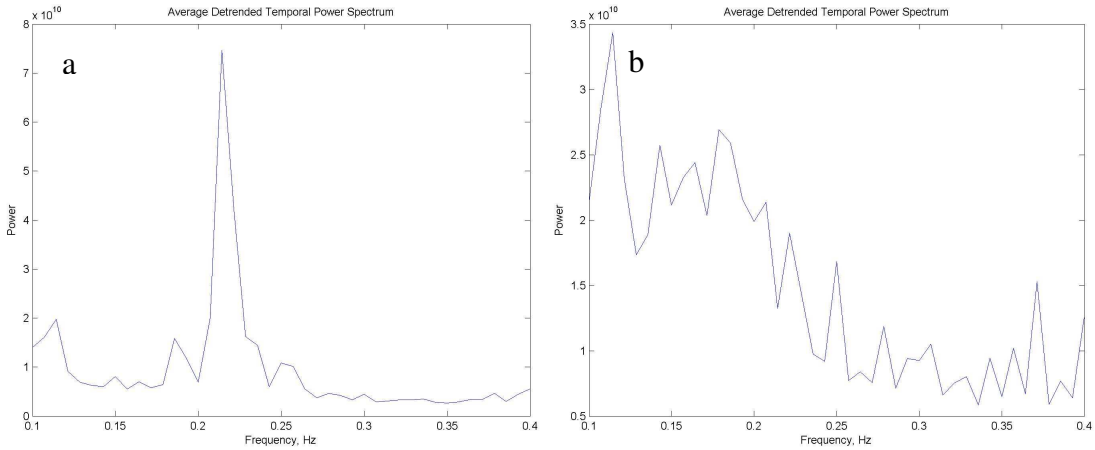

Figure 22. Mean power spectra for all brain pixels in one subject a) normal breathing and b) breath holding.

In the spectra of individual normal breathing and breath hold blocks, normal breathing blocks exhibit a clear respiratory peak while breath hold blocks do not.

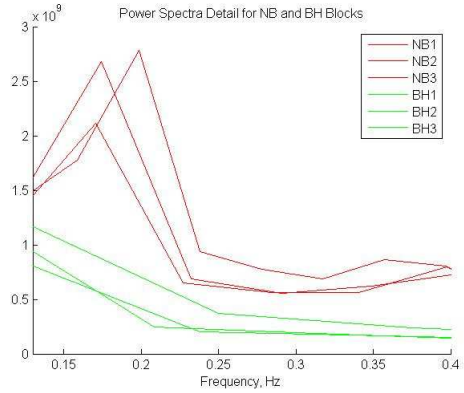

Figure 23. Power spectra for normal breathing (red) and breath hold (green) blocks on one acquisition.

Thus, during breath-hold blocks pixels do not exhibit fluctuations at respiratory frequencies and again we see reduced fractional respiratory power corresponding to higher tSNR. Though there was no significant difference in mean signal between periods of normal breathing and breath holding, there was a small (~2.0%) but consistent reduction in total variance during breath hold intervals independent of SENSE factor.

To better visualize image-to-image signal stability, we investigated 'sliding variance,' or the variance within a window (here +/- 2 dynamics scans) about a given scan; e.g. sliding variance for a pixel in image 20 would that pixel's variance over images 18 through 22.

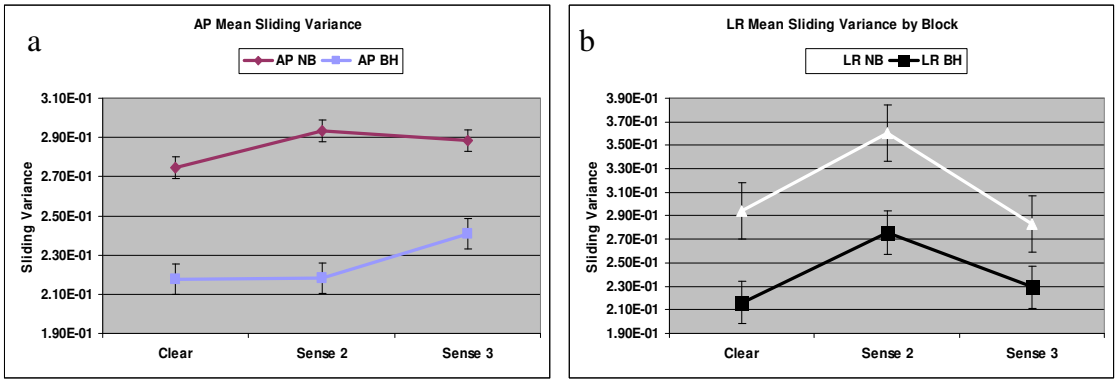

Figure 24. Mean sliding variance within breath hold and normal breathing blocks for all subjects in (a) AP and (b) LR acquisitions.

Mean sliding variance for normal breathing blocks is larger (27% AP; 30% LR) than that of breath hold blocks, though at higher SENSE (R=3) this difference decreases to 7%. Sliding variance was calculated both for all brain pixels as well as only pixels strongly influenced by respiratory frequencies; the results were identical, evidencing that respiratory fluctuations are a primary source of image to image variance.

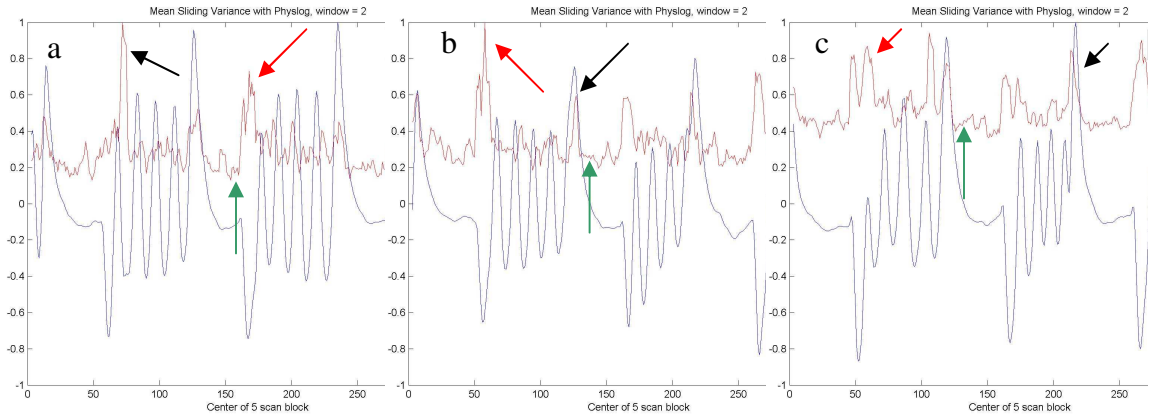

Figure 25. Normalized mean sliding variance (red) with measured physiology (blue) for AP breath hold acquisitions with (a) Clear (b) R = 2 and (c) R =3 for the same individual study. Black and red arrows indicate sliding variance increases due to inhale/exhale; green arrows indicate periods of low variance due to breath-hold.

Sliding variance increases most when a deep breath has just been taken (black arrow) or released (red arrow). As R increases, baseline sliding variance across the entire time course (green arrow) increases linearly for both normal breathing (0.98) and breath hold (0.79):

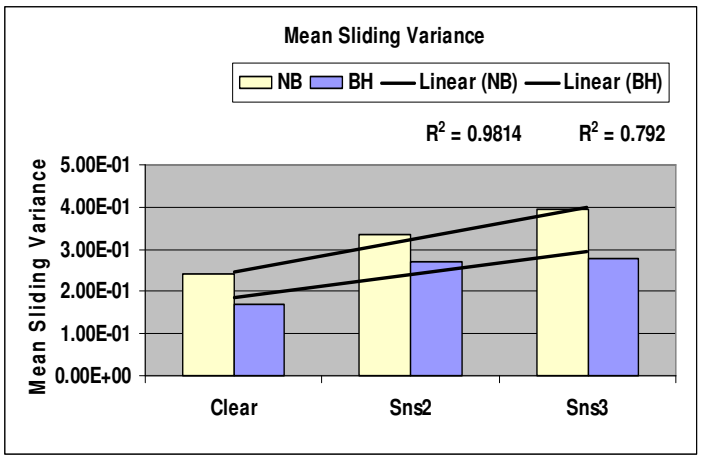

Figure 26. Mean sliding variance values for normal breathing and breath hold blocks corresponding to the sliding variance plots above. Trend lines demonstrate linear increases in sliding variance with increasing R.

This result concurs with fractional respiratory power increasing linearly with SENSE. Taken together, they suggest SENSE increases the fractional contribution of

respiratory power to the total power spectrum, which in turn increases image-to-image variance, reducing signal stability or temporal SNR.

Previous work has shown a slice position dependence of physiology-related effects. Here we further investigate the behavior of respiratory power, its interactions with SENSE, and their combined effects on tSNR as a function of distance from the lungs.

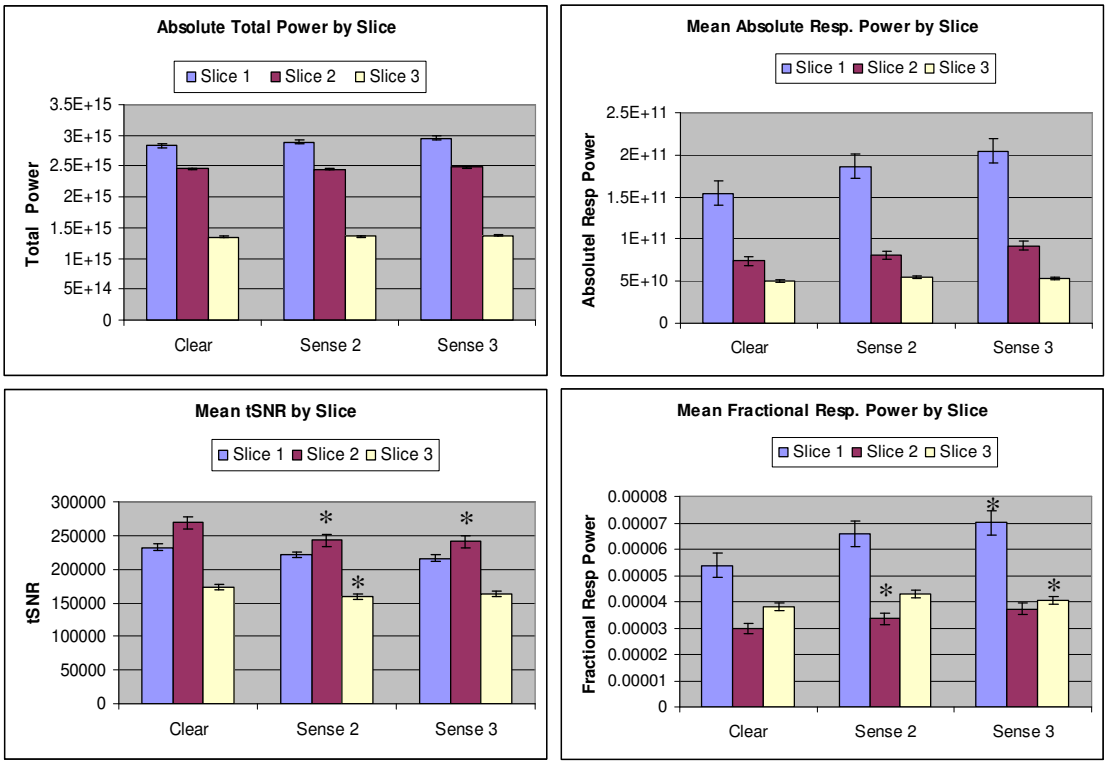

Figure 27. Relative contribution of fractional respiratory power to tSNR for an AP normal breathing acquisition. Absolute respiratory and total power are significantly decreased by the application of SENSE, but their ratio continues to increase. Asterisks indicate significant difference from CLEAR ($p < 0.05$).

As above, fractional respiratory power increases and tSNR decreases monotonically for each slice as SENSE increases. tSNR values for each slice are significantly different from one another ($p < 0.05$), though not necessarily so from one SENSE condition to the next.

Slice 1 exhibits significantly more respiratory power than slices 2 or 3 and exhibits monotonic increases in respiratory power and tSNR (mean $R^2 = 0.9679$; slice 2 $R^2 = 0.8447$; slice 3 $R^2 = 0.5263$). We also see a linear dependence of lung proximity for respiratory power and tSNR for these three slices.

Note that slice 2 has the smallest fractional respiratory power and, correspondingly, the highest tSNR. Slice 1 however, has by far the largest respiratory power but its tSNR, while significantly lower than that of slice 2, is not the lowest. Thus we see there must be other factors involved in determination of tSNR (such as field homogeneity, shim, magnet bore, slice location & thickness). If fractional respiratory power were the sole determinant of tSNR, the tSNR for slices 2 and 3 would be close together, and both much higher than that of slice 1.

As important as it is to quantify the behavior of tSNR in the slice select direction, understanding the distribution of tSNR in a set of 2-D images is even more critical. tSNR maps aid visualization of the spatial properties of tSNR as a function of SENSE.

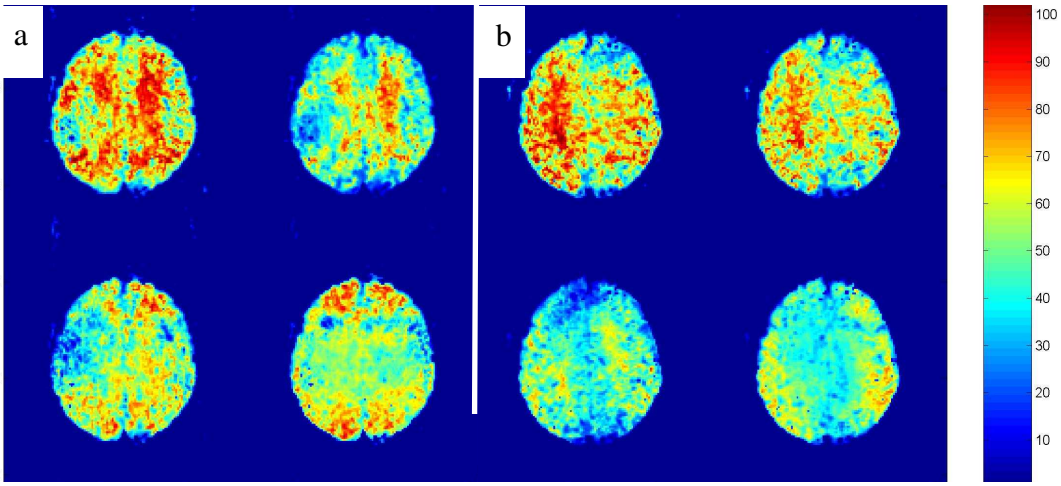

Figure 28. tSNR Map blocks for a) AP and b) LR acquisitions. Each block of 4 images is laid out: [No Sense, CLEAR; R = 2, R = 3]

tSNR decreases most rapidly in the center of field of view. As SENSE increases, *g* factors grow in the center of images due to errors in coil sensitivity measurements. High *g*-factors lead to reconstructed images with low intrinsic SNR where *g* was high (i.e. the center). A series of images with low-intrinsic-SNR will also have low tSNR because the value of a given pixel is more likely to change from one image to the next.

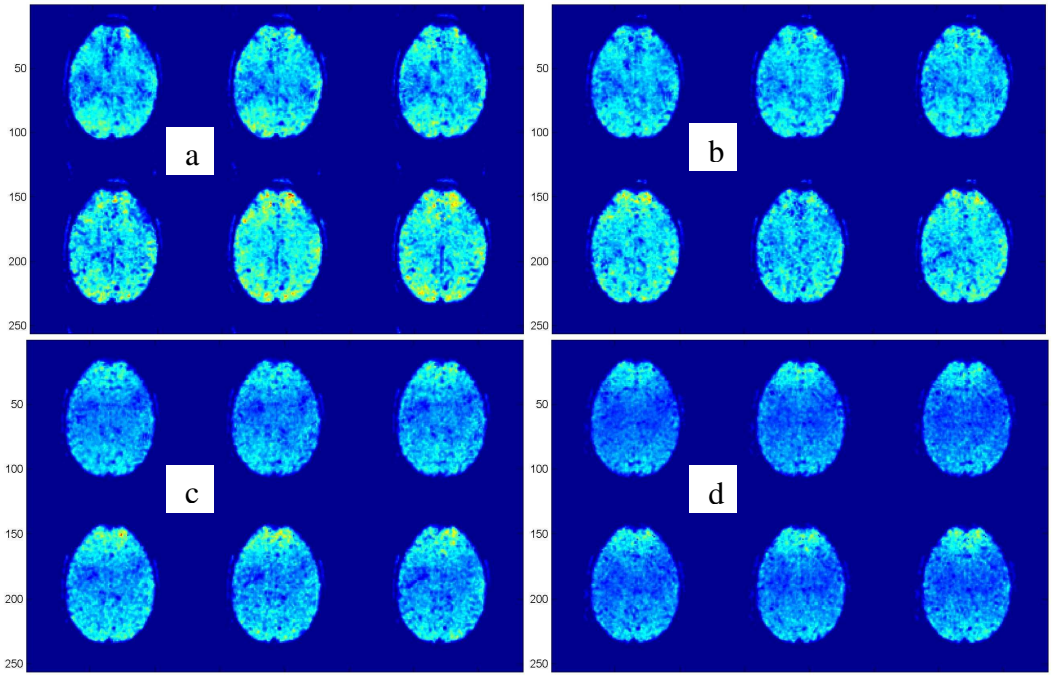

Figure 29. tSNR maps generated from AP phase encode breath-hold acquisitions. Each block of 6 images corresponds to an acquisition with a different SENSE factor. a) No Sense; b) Clear; c) R = 2; d) R = 3. Within each block, the top three images are tSNR images during normal breathing blocks, and the bottom three images are those generated during breath hold blocks.

tSNR is clearly higher throughout the brain during breath hold blocks (bottom three images in each group of six), though all images suffer from reduced tSNR in their center as SENSE increases. As above, LR acquisitions exhibit higher mean tSNR than AP acquisitions for normal breathing blocks (5%) and breath hold blocks (7%).

tSNR differences between normal breathing and breath hold blocks decreases as SENSE increases. This suggests images becoming more dominated by intrinsic noise than physiological noise at high R, a point which has implications for the second part of this research.

Discussion: Contributions of Respiratory Power to Temporal Signal Stability

In this section we have demonstrated a direct relationship between fractional respiratory power and temporal signal to noise. Fractional respiratory power increases with SENSE and has a direct, monotonic relationship with distance from the chest. tSNR is higher during periods of breath-hold than normal breathing, a result of reduced image-to-image variance by way or reduced respiratory power. Finally, tSNR decreases most quickly in the center of SENSE images, where *g* factors are higher and coil sensitivity profiles are less reliable. This leads to unstable signal in a series of image reconstructions.

A number of questions are raised by these results. We observed the middle slice exhibited the least fractional respiratory power (even though it was closer to the chest than Slice 3) and better tSNR than either of its neighbors. And even though Slice 1 was closest to the chest and featured much more respiratory power than Slices 2 or 3, its tSNR was not proportionally lower. This suggests other factors determine the initial value of tSNR, only after which the relationships defined above determine how the values change.

Image sets acquired with the LR phase encoding scheme consistently demonstrated higher tSNR than those acquired with AP phase encoding. Head motion associated with breathing generally occurs in the AP direction—parallel to the motion of the chest wall. LR acquisitions may exhibit better temporal stability because

susceptibility- and motion-related effects are orthogonal when the phase encoding direction is LR; i.e. the effects are separate and do not interfere with one another. When the phase encode gradient is along the AP direction however, head motion and susceptibility effects overlap, adding additional, unstructured image-to-image variability.

We have defined a simple, specific relationship between fractional respiratory power, sensitivity encoding, and temporal signal stability. In the second part of this research, we apply understanding of the behavior of respiratory-related susceptibility effects to a new technique for their estimation.

Motion of Center of Mass as a Respiratory Estimator

One way susceptibility effects manifest is by shifting image intensity in the phase encoding direction (Raj et al. 2001). The center of mass (COM) of an image is determined based on pixel intensity distribution in the imaging plane. Thus, if image intensity is shifted or fluctuates in some way, the location of the center of mass is affected. Raj et al. demonstrated that the time course of an image's center of mass exhibits significant fluctuations at the respiratory frequency; therefore the motion of the center of mass through time should be correlated with respiration.

Specific Methodology

We acquired each protocol (normal breathing and breath hold for each of No Sense, CLEAR, R = 2 and R = 3) with phase encoding in the AP and then LR directions. After initially processing the image data as described above (masking, detrending, normalization), center of mass for each image in the time series was calculated:

$$y_{cm} = \frac{\sum_{x=1}^{N}\sum_{y=1}^{N} I(x,y)\,y}{\sum_x \sum_y I(x,y)} \qquad x_{cm} = \frac{\sum_{x=1}^{N}\sum_{y=1}^{N} I(x,y)\,x}{\sum_x \sum_y I(x,y)} \tag{44}$$

Power spectra for the center of mass motion through time were calculated, and peaks were observed at the respiratory frequency in the COM coordinate associated with the phase encoding direction (y for AP; x for LR).

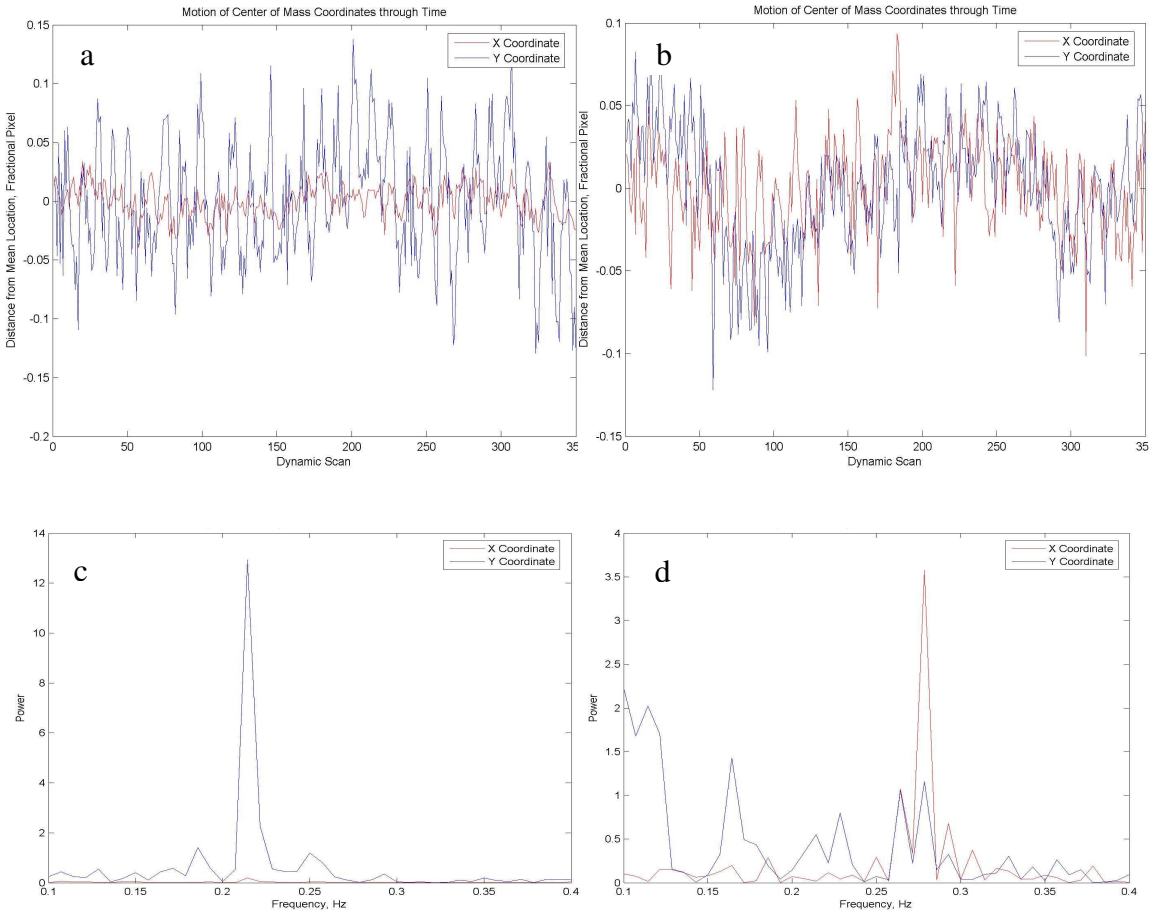

Figure 30. Motion of x (blue) and y (red) COM coordinates through time for a) AP normal breathing acquisition; b) LR normal breathing acquisition; and (c) Power spectrum for (a); (d) Power spectrum for (b)

In addition, the y-coordinate exhibited small respiratory fluctuations even when the phase encoding direction is LR. This peak is likely associated with real head-motion due to respiration (Figure 30d).

The dominant respiratory frequency was selected from a histogram of the number of pixels exhibiting high relative power at respiratory frequencies (0.1-0.4 Hz):

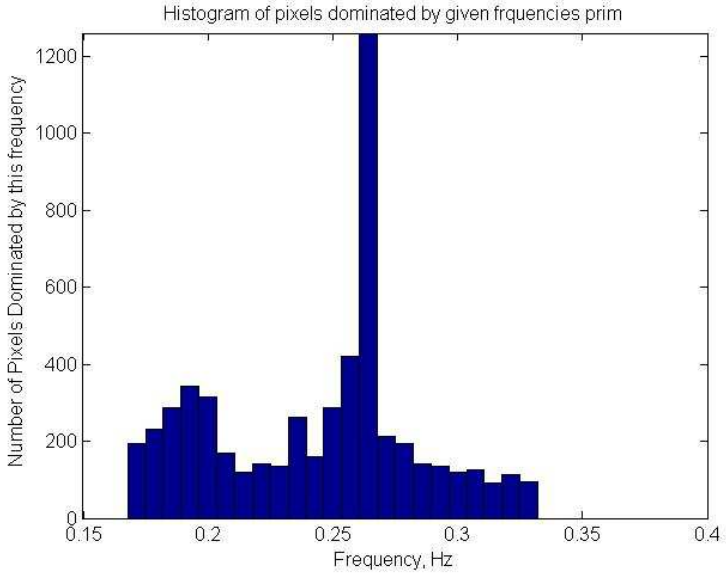

Figure 31. Representative histogram showing number of pixels dominated by a particular frequency. Finding this peak frequency, here ~0.26 Hz, allows determination of the appropriate filter range.

Once the respiratory frequency was determined, we proceeded in two ways. One was to rank all brain pixels according to the respiratory frequency's contribution to their power spectra. Time courses of the pixels with the largest such power were filtered about the peak frequency (4^{th} Order Butterworth filter), and these filtered time courses were averaged to generate the 'estimated respiratory waveform.' This estimate was then compared to the measured respiratory waveform. This method is essentially identical to the IMPACT method described above (Chuang et al., 2001).

The other method involved only the data set's center of mass. The motion of each coordinate of the COM was compared to the measured respiratory waveform with and without filtering (4th Order Butterworth) about the peak respiratory frequency.

Results: Raw Motion of Center of Mass as a Respiratory Estimator

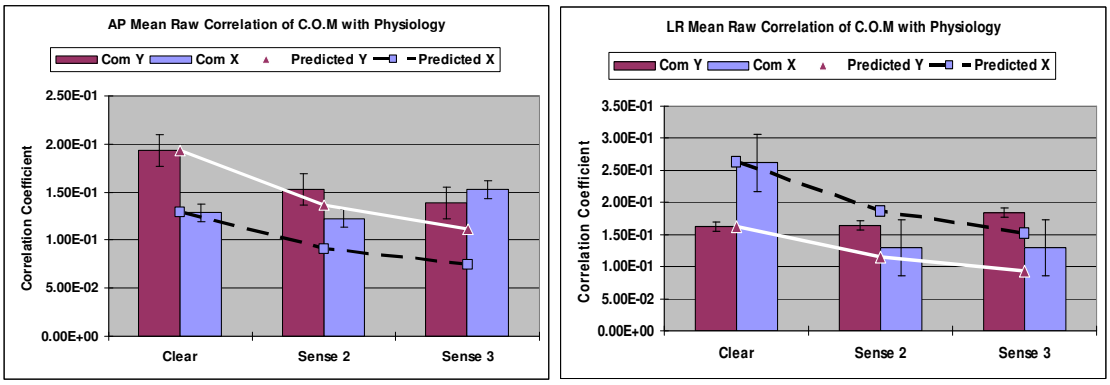

Figure 32. Correlations between raw center of mass coordinate motion and externally monitored respiration for a) AP and b) LR normal breathing studies with predicted SNR drops based on SENSE.

We observe modest correlations between monitored respiration and unfiltered motion of the COM in the phase encoding direction. As R increases, these correlations decrease in a manner that is suggestive of, but generally better than (12% at R = 2; 24% at R = 3 for AP studies), the $\frac{1}{\sqrt{R}}$ drop predicted by SENSE theory.

For both AP and LR acquisitions, respiratory estimates derived from the COM coordinate *not* associated with the phase encoding direction, while exhibiting lower correlations with respiration in general, actually get *better* as R increases. Prediction based on SENSE alone is significantly exceeded at R = 2 (35% AP; 43% LR) and R = 3 (106% AP; 97% LR).

In general, correlations for *both* the x- and y- coordinates of the COM are better for LR acquisitions. In particular, for the CLEAR LR condition the x-coordinate achieves a 36% better result than the y-coordinate for the CLEAR AP condition.

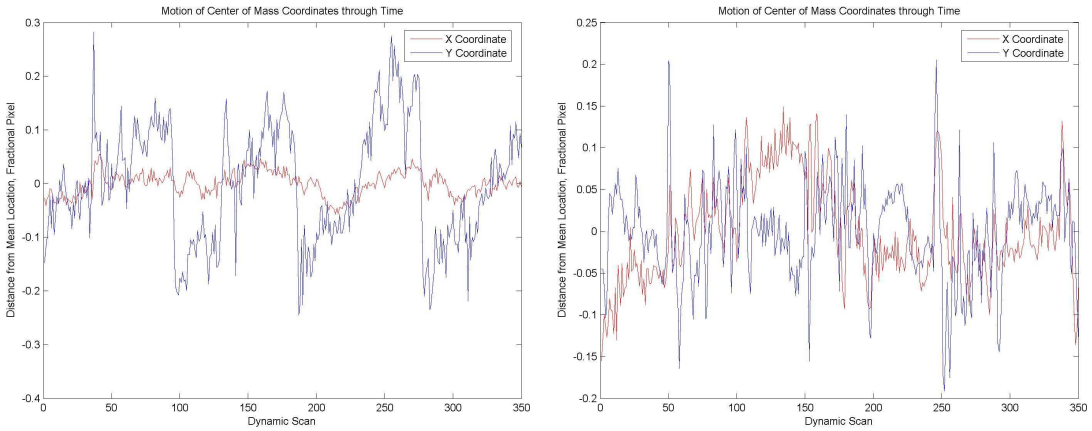

Figure 33. Motion of the x- and y-coordinates of the center of mass through time for a) No Sense AP breath hold acquisition; b) No Sense LR breath hold acquisition.

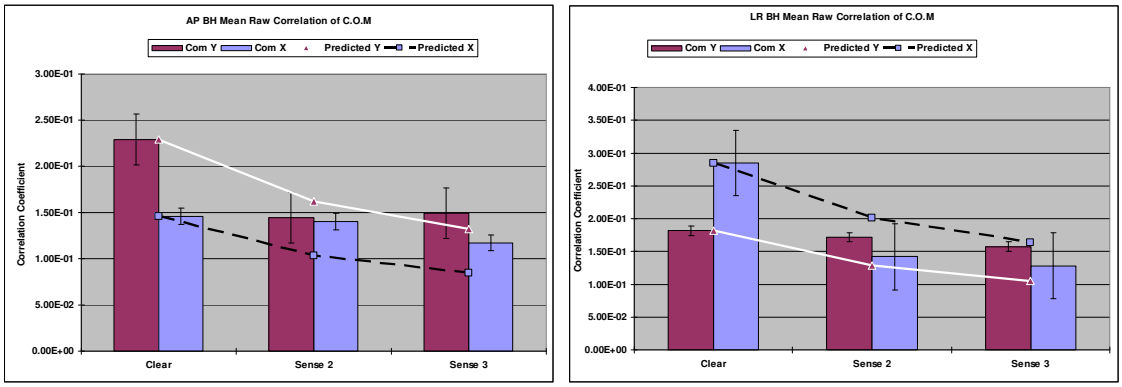

Figure 34. Correlations between raw center of mass coordinate motion and monitored respiration for a) AP and b) LR breath hold acquisitions with Predicted SNR drops based on SENSE alone ($\frac{1}{\sqrt{R}}$).

Breath-hold studies same pattern. The COM coordinate associated with the phase encoding direction exhibits significant correlations with respiration which decrease as R increases. Mean correlation values are higher (18% for y- in AP and 9% for x- in LR

acquisitions) for breath-hold studies than normal breathing studies; this suggests raw COM coordinate motion is capable of tracking breath-holds. As before, correlation magnitudes for LR acquisitions are generally higher than for AP acquisitions.

Results: Comparing IMPACT to filtered center-of-mass-based methods

The IMPACT method uses the filtered time-courses of 100 pixels with high respiratory power to estimate the respiratory waveform. The second, new method, involves filtering the motion of the center of mass through time to directly obtain the respiratory estimate. We wanted to compare these methods directly, but first we investigated the effect of using different numbers of pixels with IMPACT. Presumably, using more pixels would improve the correlations between the filtered pixel time-courses and respiration.

Respiratory waveforms were estimated from one pixel to three hundred pixels using IMPACT; each was compared to monitored physiology. Figure *35* shows correlation coefficients on the y-axis and pixels used on the x-axis for two slices of random subjects.

No correlation exists between the number of pixels used and the quality of the result; thus, there is no 'magic number' of pixels that will always result in strong correlations between pixel time courses and externally monitored respiration. And, unfortunately, the only way to tell if the respiratory waveform estimated from a given number of pixels *is* good is to compare it to monitored data.

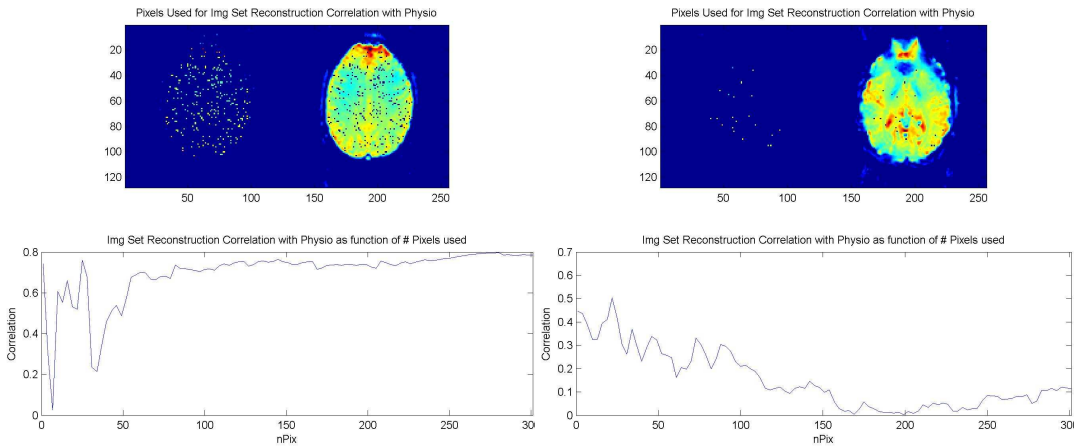

Figure 35. Maps of pixels used for maximum correlation (top), and correlation as a function of pixels used (bottom) for different slices of different subjects.

But requiring monitored data invalidates the primary suggested strength of IMPACT—that it can operate independently of such data. To compare IMPACT to the COM-based method, we chose the best possible correlation value out of all 300 for each trial. In this way we obtained very high correlations with monitored physiology regardless of phase encoding scheme or SENSE factor for IMPACT-style analysis.

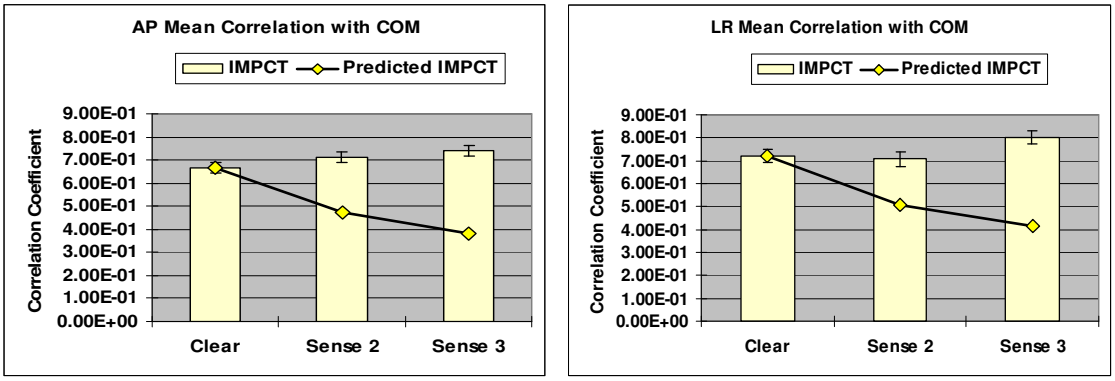

Figure 36. Mean correlation values between an optimum number of pixel time courses and an externally monitored respiratory waveform for (a) AP and (b) LR acquisitions. The line is the 'predicted' decrease in correlation if it depended on SENSE.

Optimized correlation values increase roughly linearly (R^2 = 0.98 AP; R^2 = 0.63 LR) as R increases, similar to the increase of fractional respiratory power with R above. As before, LR studies average higher correlations (5%) than the corresponding AP values.

In figure 36, solid lines show what the correlation values 'would be' if they depended on the intrinsic SNR of images acquired with SENSE; clearly IMPACT-style correlations are independent of intrinsic SNR. Instead, IMPACT's correlations are based on respiratory power in pixel power spectra; therefore these correlations are influenced by fractional respiratory power over intrinsic SNR.

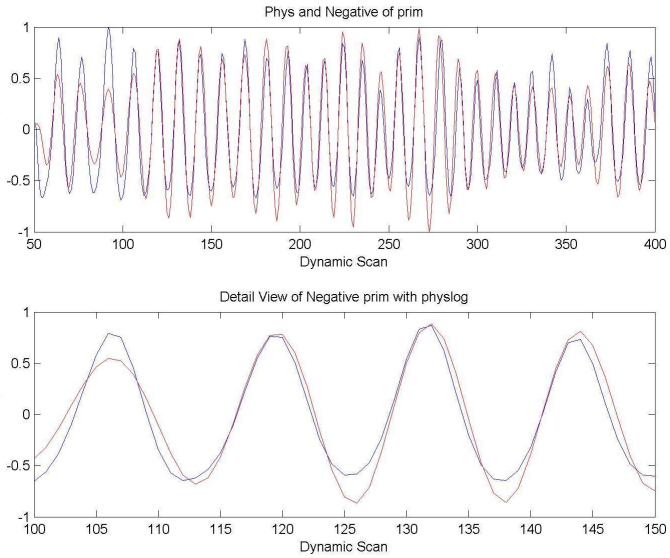

Figure 37. Externally monitored (blue) and optimized IMPACT-estimated (red) respiratory waveforms.

Using the center-of-mass method, correlations between the filtered motion of the COM coordinate associated with the phase encoding direction and monitored respiration decrease linearly (R^2 = 0.97 AP; R^2 = 0.90 LR) as R increases. In both cases, the mean correlation value seems to loosely follow the $\frac{1}{\sqrt{R}}$ dependence of intrinsic image SNR due to SENSE, though mean y-correlations for AP are significantly better (22% better at R =

2 and 37% at R = 3) than predicted; x-correlations for LR acquisitions almost exactly predicted values (92% of prediction at R = 2; 96.2% of prediction at R = 3).

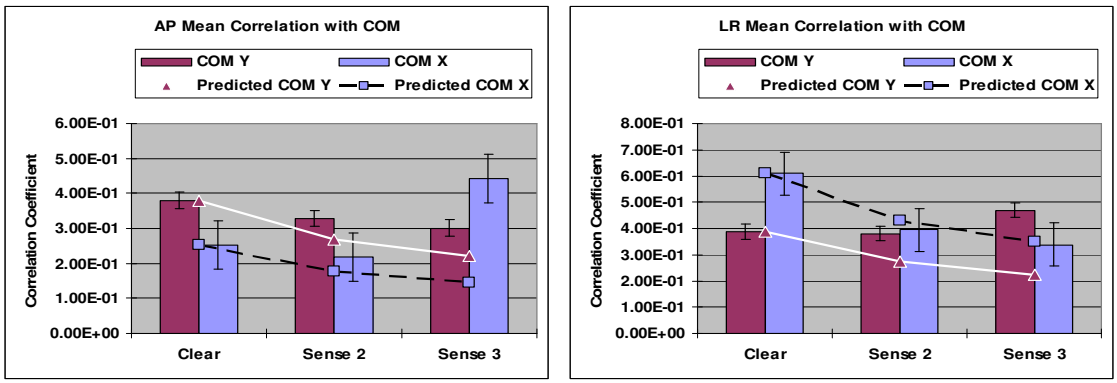

Figure 38. Mean correlation values between an optimum number of pixel time courses and an externally monitored respiratory waveform for (a) AP and (b) LR acquisitions. The line is the 'predicted' decrease in correlation if it depended on SENSE.

As with the unfiltered data, the COM coordinate *not* associated with the phase encode direction becomes increasingly correlated with respiration as R increases (x: 22% better at R = 2, 303% at R = 3 for AP, and y: 39% better at R = 2, 210% at R = 3 for LR).

This suggests COM-based methods depend on a combination of respiratory power (in the spectrum of the desired COM coordinate), as well as the intrinsic SNR of each image (as determined by SENSE and other factors). Higher fractional respiratory power leads to stronger correlations with respiration independent of image SNR or of phase encoding direction.

Thus, in the center-of-mass method competition exists between the correlation-deteriorating effects of SENSE-based intrinsic SNR loss, and the correlation enhancing effects of SENSE-based fractional respiratory power boosts. We can view correlations from the IMPACT-based and COM-based methods together in figure 39:

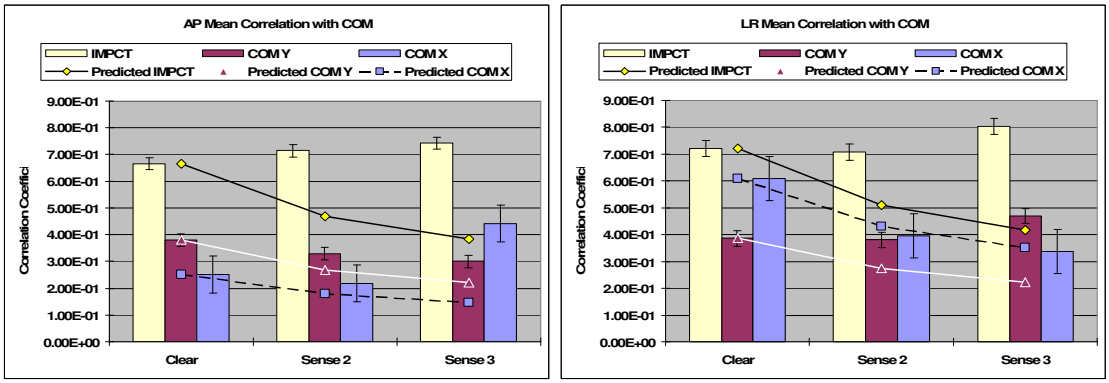

Figure 39. Mean correlation values for both methods for respiratory waveform for (a) AP and (b) LR normal breathing acquisitions. The line is the 'predicted' decrease in correlation if it depended on SENSE.

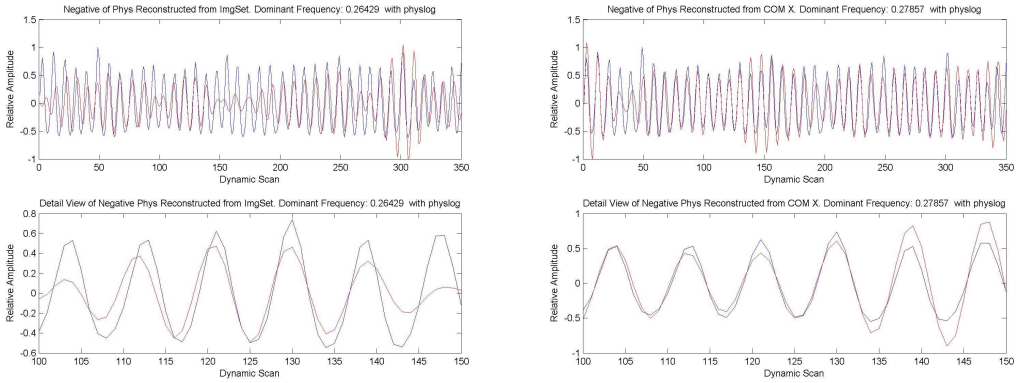

Figure 40. Estimated Respiratory Waveforms for Optimized IMPACT and the x- coordinate of the center of mass for an LR study of the same subject acquired without SENSE.

It has been shown that correcting for respiratory depth can reduce time course signal variance by at least a further 10% compared to the same method without such corrections (Chuang et al. 2001). COM-based methods approximate respiration depth more accurately than IMPACT (Figure 40); this is not evident in pure correlation numbers. Though the IMPACT method *can* estimate respiration depth, doing so requires external monitoring, extra coding and extra processing. Because center of mass displacement depends on susceptibility effects (which are a function of respiration depth), the center-of-mass method implicitly includes this information for 'free.'

With breath hold data we observe uniformly reduced correlation magnitudes for both IMPACT and COM-based methods. These values are quite different from what we observed in the raw breath-hold data above—the key difference here is filtering. Breath hold studies distribute respiratory power much more evenly across the respiratory range than normal breathing studies (see Figure 22), invalidating the concept of an identifiable 'peak' respiratory frequency as a guide for filtering.

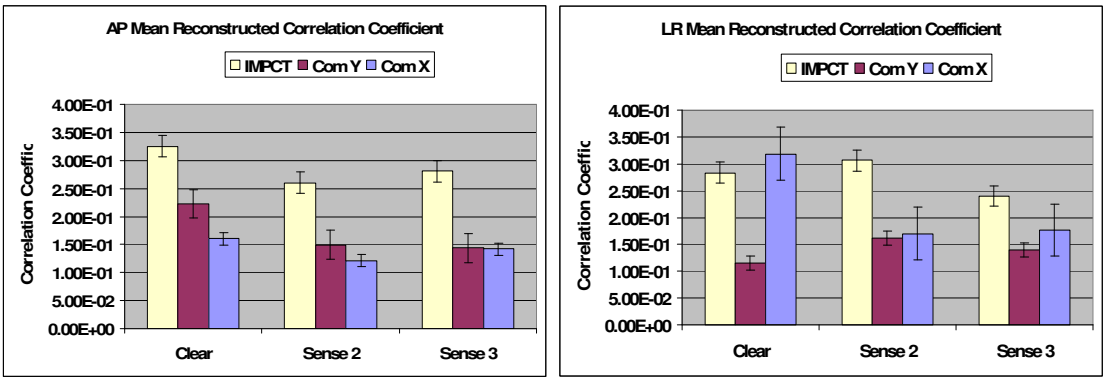

Figure 41. Mean correlation values for both methods for respiratory waveform for (a) AP and (b) LR breath-hold acquisitions for both IMPACT and COM-based estimation methods.

Thus, even if there is good agreement during the 'normal breathing blocks' of a breath-hold study, the difficulty in estimating breath-hold events all but insures low overall correlation values.

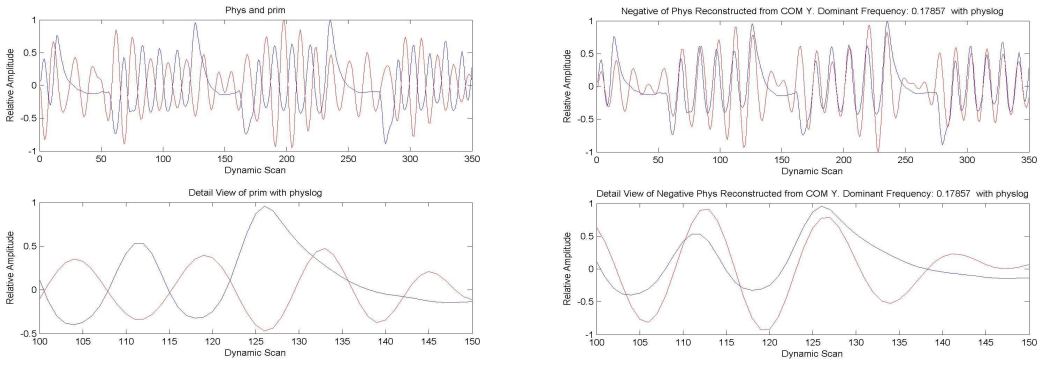

Figure 42. Estimated respiratory waveforms for a breath-hold study. Though there is good agreement during the normal-breathing parts of the time course, breath-hold events are very poorly estimated, with IMPACT resulting in a low correlation coefficient. The COM method does a better job of estimating the breath-hold intervals than IMPACT.

Despite this, for the breath-hold CLEAR LR, the COM x-coordinate actually provides 13% better correlation with measured respiration than the optimized pixel-search IMPACT method is capable of.

Though on average optimized IMPACT provides generally better estimates than COM-based methods for normal breathing and breath-hold studies, correlations obtained in this way for breath-hold studies behave differently from normal breathing studies namely, they do not improve as SENSE increases. This can be attributed to the lack of a well-defined respiration frequency, which makes 'increasing fractional respiratory power' difficult to quantify.

Discussion: Motion of Center of Mass as a Respiratory Estimator

In this section we have discussed two methods for estimating the respiratory waveform from image data. The first, IMPACT, was developed by Chuang et al. with the intention of estimating and correcting respiratory artifacts without monitored physiological data. We validated this method, but also demonstrated its sensitivity to the spectral content of the pixel time courses used to estimate the respiratory waveform. Thus, following the original paper's recommendation of using the 100 pixels with the most respiratory power seems ill-advised; the optimum pixel number varies in unpredictable ways which prevents reliable use of the technique without external monitoring.

In order to achieve reliable correlations with IMPACT we implemented an optimization scheme wherein 300 estimates of the respiratory waveform were prepared and compared to an external estimate. This allowed for consistently high estimates of the

respiratory waveform, but it required externally monitored data, invalidating one of the primary benefits of using IMPACT according to Chuang et al.

One way to overcome this without externally monitored data would be to generate a number of estimated waveforms, apply corrections for all of them, and choose the one which most reduced image to image variance. While this could work, it would be computationally intensive and inelegant.

Thus, based on knowledge that respiration-related susceptibility effects manifest as image shifts in the phase encoding direction, we proposed a new method which uses the motion an image's center of mass through time as an estimator for the respiratory waveform. Using the center of mass instead of individual pixel time courses has a number of advantages. Computationally, it is several orders of magnitude faster than the optimized IMPACT approach (0.03 seconds vs. 15 seconds—500 times faster). Even compared with IMPACT using 100 pixels as per the literature, the center of mass technique is still almost 23 times faster (0.69 vs. 0.03 seconds).

Though in general the respiratory waveforms generated with the optimized IMPACT method yielded better correlations with physiology than did those generated with the center of mass approach, the optimized IMPACT method implemented here was more for the sake of testing IMPACT's limits than it would be practically useful. Even so, in some cases the center of mass approach yielded correlations that exceeded the best possible values with optimized IMPACT. For example, in one subject the average optimized IMPACT correlation across all three slices was 0.245, while the average center of mass y-coordinate correlation was 0.562.

While the increasing fractional respiratory power associated with increasing R tended to increase the correlations of IMPACT method-based respiratory estimates, the decreased intrinsic SNR associated with increasing R tended to reduce the effectiveness of the COM-based methods. If the center of mass cannot be reliably calculated within a given image, then tracking its motion through time becomes difficult as well.

This intrinsic SNR-related decrease seems to be somewhat offset by a component of respiratory power involved in COM-based respiratory estimates, evidenced by respiratory estimates derived from the center of mass coordinate *not* associated with the phase encoding direction increasing as R increases while those derived from the coordinate associated with the phase encoding direction decreases.

It seems, then, that the accuracy of COM-based respiratory estimates depends on an interplay of fractional respiratory power and intrinsic image SNR, while IMPACT-based respiratory estimates depend solely on fractional respiratory power. Given that fractional respiratory power increases and intrinsic SNR decreases as R increases, IMPACT-based methods may be a good choice for correcting respiratory artifacts in data sets acquired at high SENSE factors.

The center of mass method, on the other hand, provides solid, significant correlations with respiratory processes in a fraction of the computation time and truly does not necessitate external monitoring. Since this alternate method was developed based on IMPACT, utilizes the center of mass (COM), is simpler and computationally 'smaller', we dub this new method COMPACT: Center Of Mass-based Physiological Artifact Correction Technique.

Additionally, Chuang et al. demonstrated that correcting for respiratory depth can increase the quality of the correction by over 10%, though they say that increase may not be worth extra processing involved. Because COMPACT is based on a susceptibility-effect model of respiratory effects instead of additive noise, the respiratory depth estimates are included automatically, which should result in larger variance reductions than IMPACT for respiratory waveform estimates with the same correlation coefficients.

Overall, we suggest image-space-based physiological artifact correction techniques are preferable to k-space-based methods for the following reasons:

1. fMRI activation maps are calculated from image data;
2. Processing image data is less computationally intensive than k-space data;
3. k-space data is not readily available at all institutions;
4. Correcting for respiratory effects in k-space can introduce noise correlations into pixels at similar spatial frequencies.

One concern with image-based methods in particular is the ability to distinguish between real head motion and apparent head motion due to susceptibility effects. This is especially important when acquiring images with AP phase encoding (the direction in which head motion usually occurs). We have shown that acquiring images with phase encoding in the LR direction can separate these effects and have measurable effect on the quality of the data. We also saw significant increases in tSNR and correlations between estimated and measured respiratory waveforms for almost every LR acquisition compared to its AP counterpart for both the IMPACT and COMPACT methods. Future

work will be dedicated to distinguishing this apparent vs. real motion in more quantitative and subtle ways.

Though corrections based on respiratory waveforms estimated here have not been performed, the IMPACT and COMPACT methods do not differ in that regard; both involve reordering images into unit physiological cycles, then removing noise artifacts based on the estimated respiratory waveform. The only differentiator in quality of correction is the accurate and reliable estimation of that waveform.

Summary & Conclusions

Functional MRI allows researchers and clinicians to investigate brain activity, but the technique depends on long-term time-course signal stability. Among the many sources of noise which cause temporal signal variance and interfere with fMRI detectability, respiration introduces susceptibility effects which can severely affect the temporal stability of the fMRI signal. Here we have investigated the nature and extent of respiration-induced susceptibility effects in normal breathing and breath-hold studies as a function of sensitivity-encoding reduction factor and phase encoding gradient direction.

Our results confirm that fractional respiratory power is directly related to time-course signal stability. We have determined that fractional respiratory power increases both as SENSE reduction factor increases and with proximity to the chest. In addition, temporal signal stability is improved during periods of breath hold when fractional respiratory power is reduced or eliminated.

We have investigated the spatial distribution of tSNR as a function of SENSE reduction factor, and found that tSNR losses are most severe in the center of the image where *g* factors are high and accuracy of sensitivity maps is low.

We have investigated the relative merits of k-space-based and image-space-based techniques for physiological noise removal and discovered that the usefulness of the IMPACT method depends on spectral content of individual brain pixels. Consequently, its effectiveness increases with fractional respiratory power (and therefore with SENSE).

However, sensitivity to spectral content also means there is no 'magic number' of pixels that will always provide reliable results. Instead, obtaining reliable respiratory estimates using IMPACT requires externally monitored respiratory data for comparison. Though this is not necessarily a problem, it does limit IMPACT's usefulness; the method was originally touted as not requiring monitoring. Further, it prevents retrospective application of the technique to studies without such monitoring.

In light of this, we have offered an idea to improve upon IMPACT in terms of efficiency, simplicity, and the ability to estimate physiological effects truly without external monitoring. This method, COMPACT, uses the motion of an image's center of mass through time as a respiratory estimator. COMPACT is based on knowledge that respiration-related susceptibility effects manifest as image intensity shifts which change the location of the image's center of mass.

Compared to IMPACT, COMPACT is a faster, simpler, more generally applicable means of estimating the respiratory waveform from image data. Further, this method truly does not require external monitoring of or synchronization with physiological data, and could be retrospectively applied with ease to all existing fMRI data sets.

Perspectives & Future Work

A wealth of possibilities follow from this work. First is implementing the physiological artifact correction scheme in COMPACT. That work is underway, and will eventually include corrections for cardiac effects and analysis of real functional MRI data.

In the future, dedicated fMRI data could be acquired at 3T and 7T and analyzed with the techniques presented here. Since EPI-related effects are expected to worsen at higher fields, we could acquire this data using several pulse sequences including single shot EPI, multi-shot EPI, and PRESTO, an MRI technique that employs echo-shifting for faster data acquisition. All protocols could be acquired with SENSE to quantify the effects of field strength and pulse sequence on the SENSE-related effects observed here.

In terms of algorithms, more experimentation can be done with specific kinds of filtering. Glover et al. (2000) suggest that since respiratory and cardiac signals are not stationary, wavelet-based filtering may perform better than traditional filters.

Other considerations not necessarily specific to these applications include the suggestion that the sign of the phase encode blips through k-space (positive or negative), may have a significant impact on susceptibility effects in EPI images, especially in deeper cortical regions such as the orbitofrontal cortex and lower temporal lobe (De Panfilis and Schwarzbauer 2005). Depending on the direction of the susceptibility-induced gradient in a particular region, either positive or negative blips yield better results. This complimentary effect could be utilized by acquiring both positively and negatively blipped images and by combining the corresponding image intensities. This is analogous to Chang & Fitzpatrick's work with reverse gradient methods for image distortion in EPI and could be considered accordingly.

Another approach to consider is multi-shot imaging. An assumption of image-based correction methods is that each image is collected at a discrete time for which unique cardiac and respiratory phases can be assigned. This is a good assumption for single shot imaging, but may not be for multi-shot acquisitions because the multiple TR periods needed for all segments may span several cardiac or respiratory cycles. In this case the k-space method, in principle, may have an advantage because each segment can be corrected separately before combination during reconstruction.

However, physiological image modulation is inherently reduced in multi-shot acquisitions, so it would be interesting to investigate this more thoroughly. Glover et al. applied RETROICOR to multi-shot Fast Low Angle Shot (FLASH) imaging and found reduction of physiological noise effects on par with those observed in single-shot scans (Glover et al. 2000).

In summary, we have validated and evolved a number of ideas surrounding the nature and behavior of respiration-related susceptibility effects both in the context of individual images and series of images through time. Further, we have demonstrated how those effects interact with sensitivity-encoded parallel imaging acquisitions and introduced a new technique for respiratory estimation from image data without physiological monitoring. This work has raised many questions, but it also provides new information about the way in which respiratory effects and parallel imaging interact and how this information can be applied. We hope the foundation laid here will lead to more powerful fMRI pre-processing techniques which will improve the usefulness of fMRI data and provide valuable insight into the delicate machinery of the human brain.

APPENDIX A

EFFECTS OF SWITCHING PHASE ENCODING GRADIENTS ON SUSCEPTIBILITY-RELATED EFFECTS

Raj et al. (2001) demonstrated, in addition to image shifting, intensity shading on the order of 1% in the phase encoding direction. They generated maps demonstrating these effects by taking the difference between the mean image of an entire time course and the mean of images associated with the peak or trough of respiration.

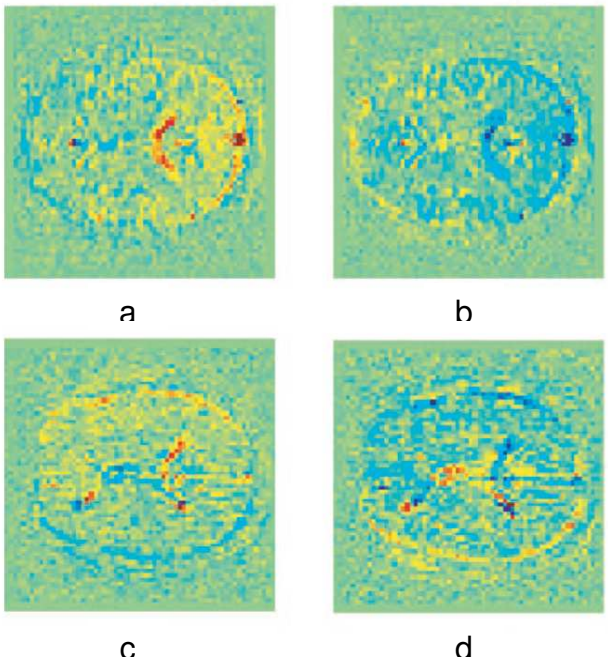

Figure 43. Intensity gradient effects observed in Raj et al. (2000). Images a) and b) difference from mean with AP phase encode; Images c) and d) differences from mean with LR phase encode. The intensity gradients follow the phase encoding direction.

We generated similar maps, but the effects we observed were slightly different. Both in our images and those generated by Raj et al., significant edge effects are visible. In fact, in our maps the edge effects are more noticeable—this is evidence of the field-

strength dependence of susceptibility-effect-based image shifting (our images were acquired at 3T while those of Raj et al. were acquired at 1.5T)

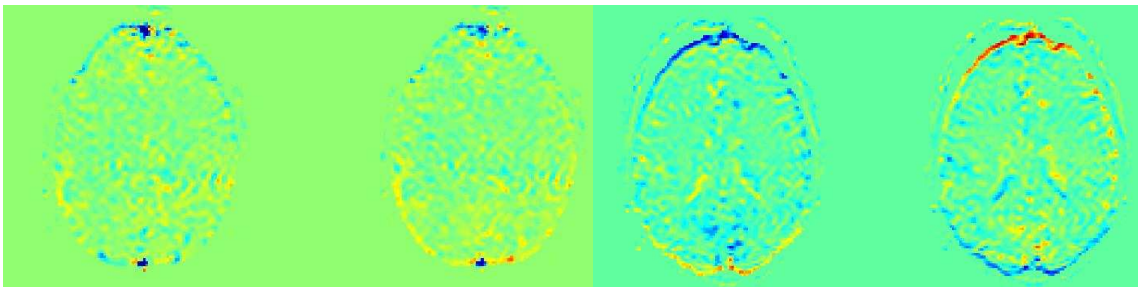

Figure 44. Difference maps of respiratory extrema compared to the time series mean image using images associated with a) respiratory extrema only b) a 10 scan window about the respiratory extrema.

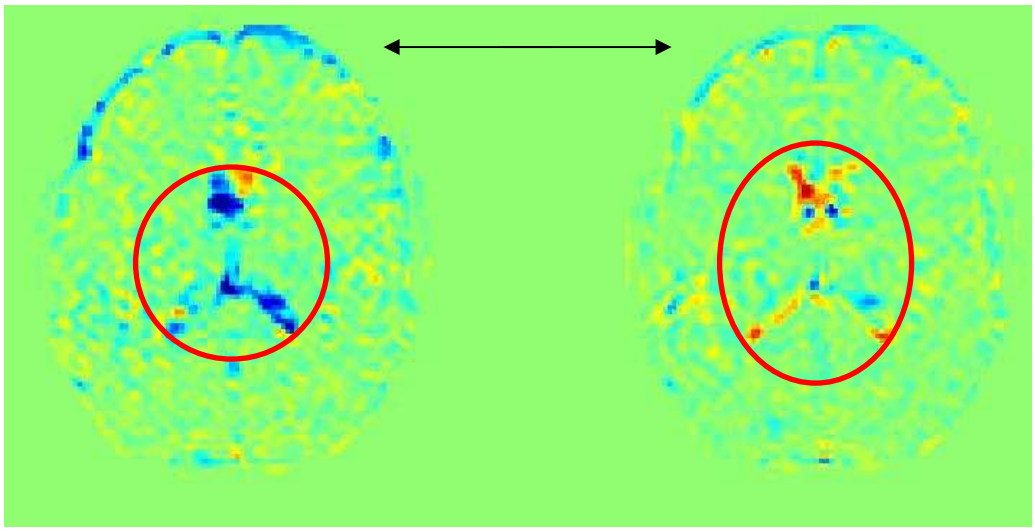

Figure 45. Detail view of a CLEAR acquisition difference map with AP phase encode. Edge effects are visible (black arrows), likely due to a susceptibility-related image shift. Inside the brain, shading effects are most clearly visible in the ventricles (red circles). The intensity gradient observed by Raj et al. (2001) is not immediately apparent.

Some intensity shading, primarily in the ventricles, and some modest edge effects were observed on difference maps created in this way. However, the intensity gradient observed by Raj et al. was not immediately apparent. We investigated these effects both under normal breathing and breath hold conditions at a number of SENSE factors.

We found increasing SENSE made the effects much more difficult to observe, creating images which were very noisy.

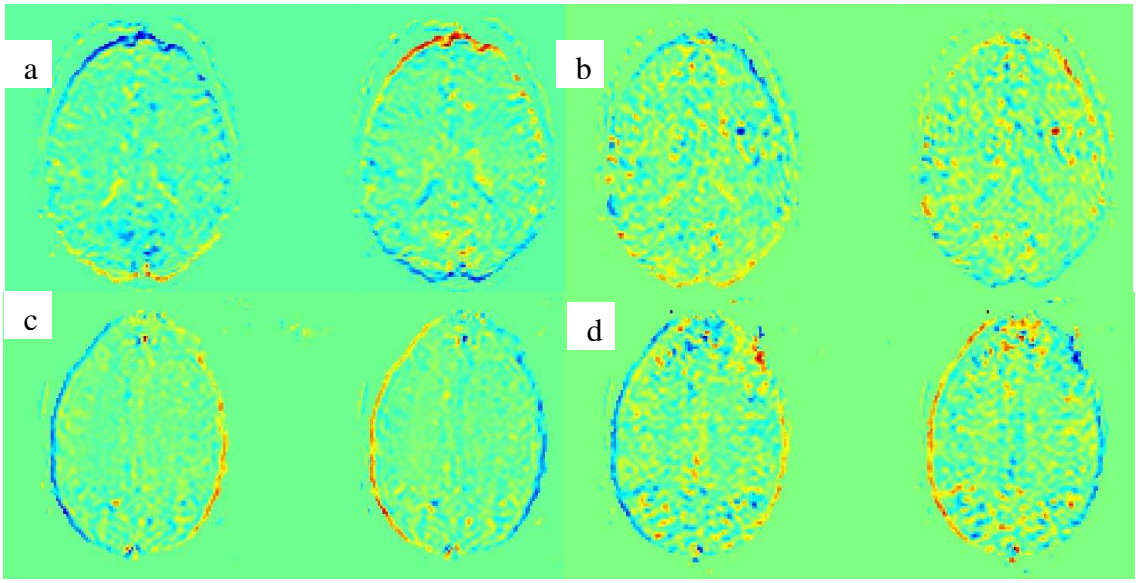

Figure 46. Intensity shading and image shift due to susceptibility. a) AP, No Sense b) AP, R = 2 c) LR, No Sense d) LR, R = 2.

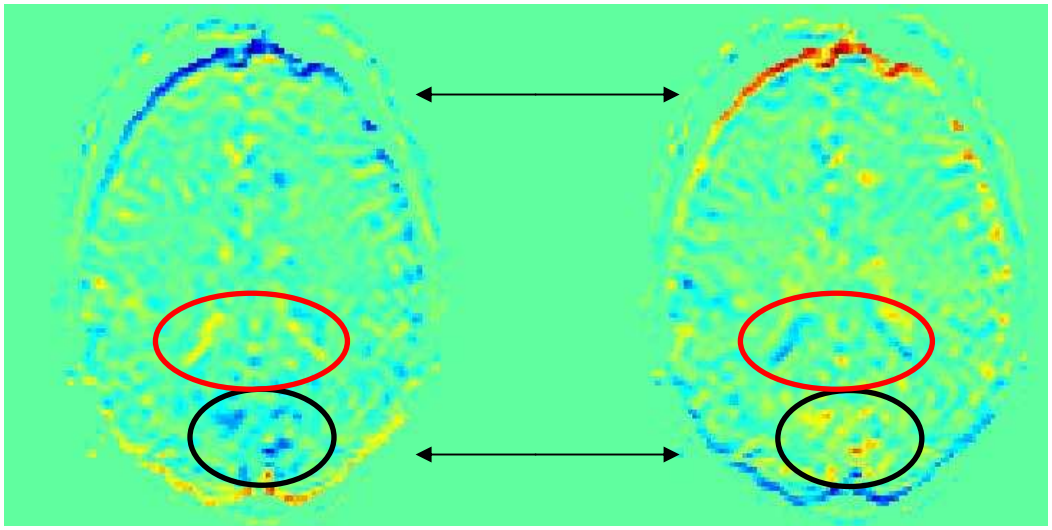
Figure 47. Detail view of a No Sense acquisition with AP phase encode (image (a) above). Edge effects are clearly visible (black arrows), likely due to a susceptibility-related image shift. Inside the brain, shading effects are most clearly visible in the ventricles (red circles) and near the back of the head (black circles). The intensity gradient observed by Raj et al. (2001) is not immediately apparent here.

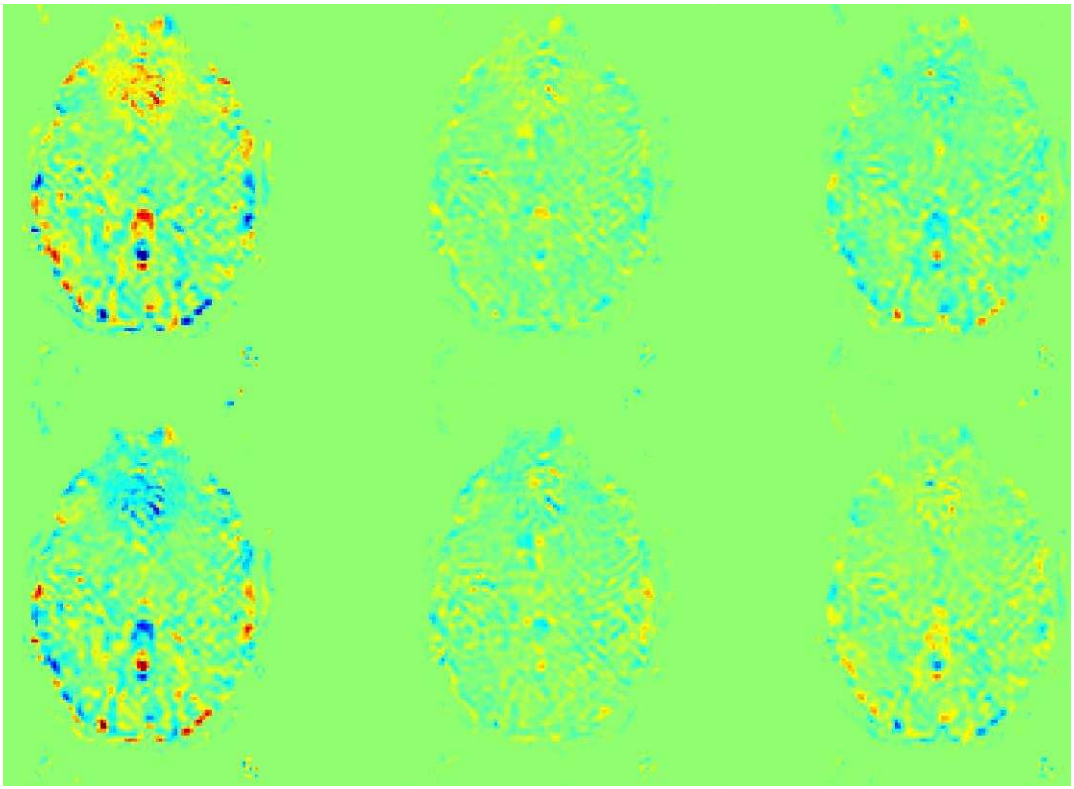

Figure 48. Respiratory extrema difference maps determined from the normal breathing blocks of slice 1 of a No Sense AP acquisition. Top row represents the difference between the block mean image of normal breathing block 1, 2, and 3 (horizontally) and the average respiratory minima image of that block, while the bottom row represents comparable differences between block average respiratory maxima images and the mean image for the appropriate block.

Looking at extrema during normal breathing blocks (about 10 TR in length) of a breath-hold study, we observed similar behavior. Observe the orbitofrontal cortex in particular. Intensity shading is extreme in the first normal breathing block, and more subtly in the second two. This supports previous findings that this area is particularly sensitive to susceptibility effects, making fMRI of that region difficult.

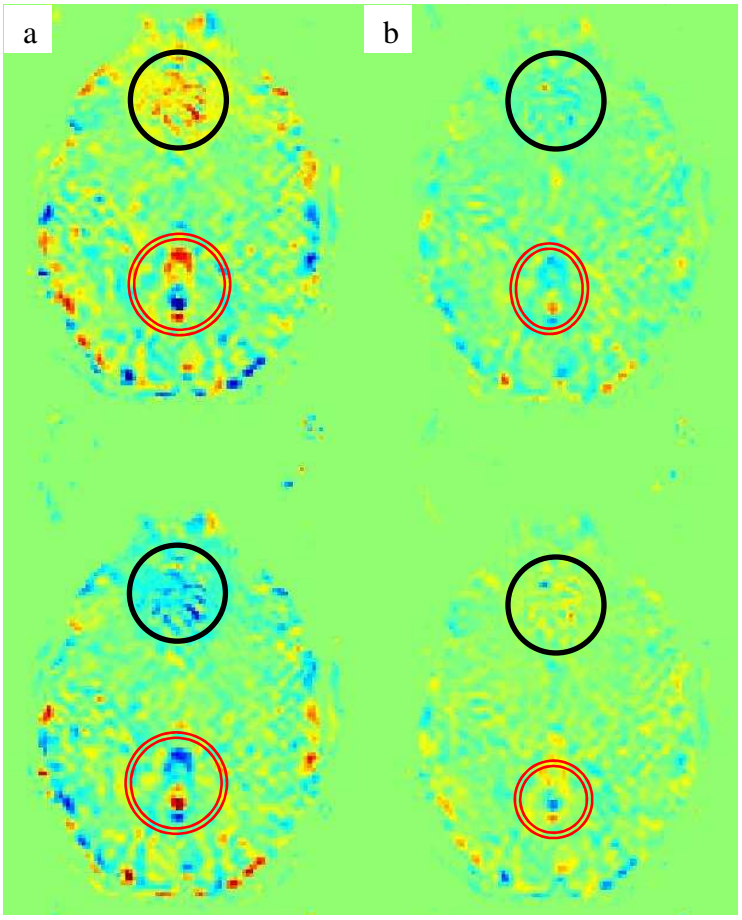

Figure 49.
Detail view of difference maps from two normal breathing blocks of slice 1 of a No Sense AP breath-hold acquisition.

Images arranged vertically; top image is mean image of respiratory maxima minus the time mean image. Bottom image is the time mean image minus the mean image of respiratory minima.

a) Normal Breathing block 1
b) Normal Breathing block 3

Notable features in the left image include the orbitofrontal cortex (black circle) and base of the ventricles (red circle). On the right set of images, the effects are more subtle. In these images, the intensity shading is clear not only on the edges of the brain, but throughout the center of the image. While an intensity gradient as per Raj et al. (2001) is not clear, a global shading effect is observed, in particular on image (b) above, and is well-illustrated in figure 50:

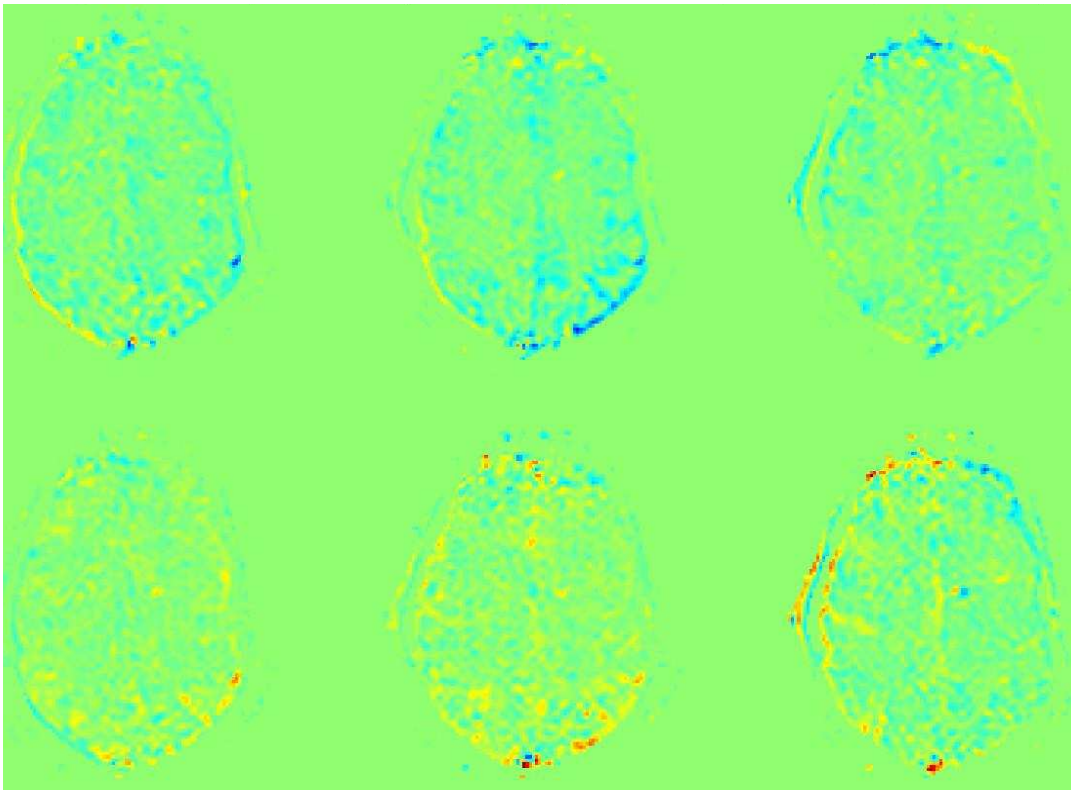

Figure 50. Respiratory extrema difference maps determined from the normal breathing blocks of slice 2 of the same No Sense AP acquisition as above. Image layout same as above.

Here we observe subtle edge effects and fairly clear global intensity shading. In general, we observe larger intensity differences on the bottom row (difference between a given block mean image and the respiratory maxima of that image). This makes sense because at respiratory peaks the lungs are full of oxygen and the chest wall is maximally displaced; this, susceptibility effects and their corresponding signal differences are expected to be more severe at respiratory peaks than troughs.

The question, then, is whether these shading effects are due to a simple image shift caused by a spatially invariant susceptibility related off-resonance effects, or something subtler. To investigate this, simulated shifted images were generated to verify the intensity patterns that result from shifting an image by 1, 2, 3 or 4 pixels in the phase encoding direction:

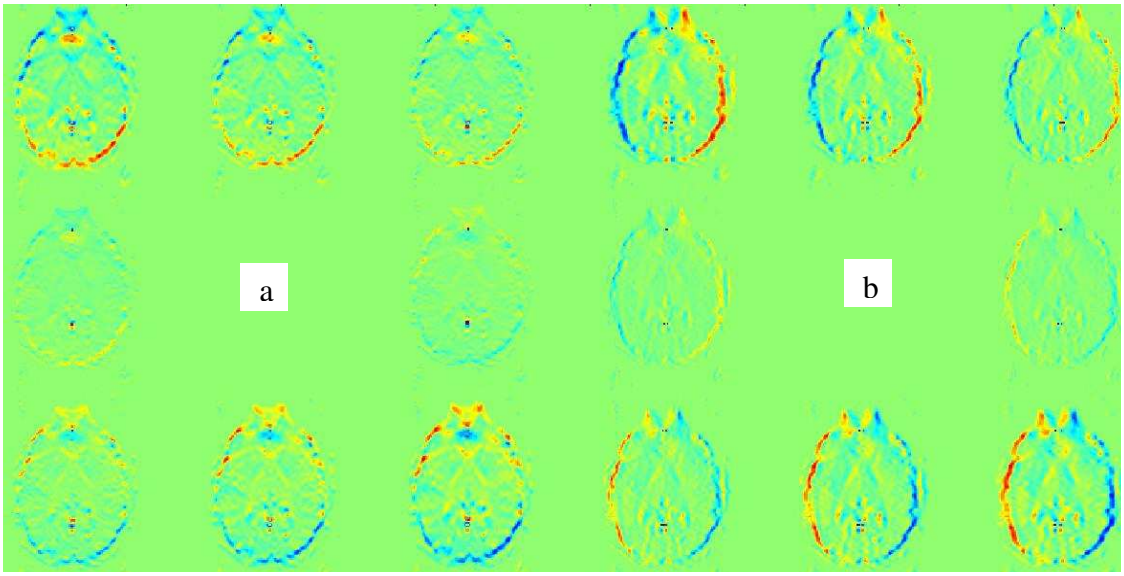

Figure 51. A set of simulated shifted images for both AP and LR acquisitions. For each set of 9 images, the top row represents a shift of 4, 3, and 2 pixels; the second row: 1, 0 and -1 pixels; the third row: -2, -3 and -4 pixels in the phase encoding direction. a) Simulated images for AP acquisitions; b) simulated images for LR acquisitions.

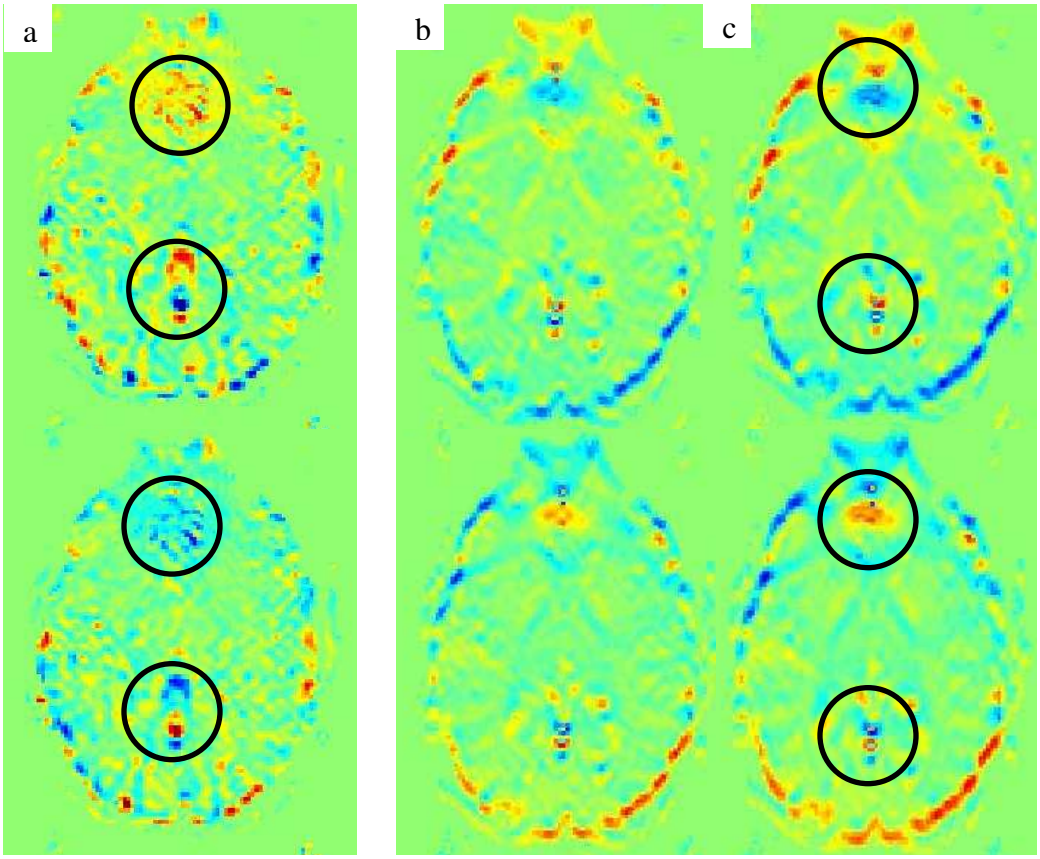

Figure 52. Comparison of measured (a) with simulated images shifted by 2 (b) and 3 (c) pixels.

Comparison of acquired to simulated images reveals similar edge effects but different shading behavior within the brain, especially in the orbitofrontal cortex (black circles); here the simulated image has both high and low intensity spots, where the real image is dominated one or the other.

All of the image artifacts in these difference maps cannot be explained by simple image shifting. Other susceptibility related effects such as local intensity displacement are likely involved, as well as other noise sources, but the extent and nature of those effects are difficult to determine from these images.

This may be due to the fact that the extrema images are generated by averaging respiratory extrema from the entire time series, while the breath hold analysis averages, by block, just a few respiratory peaks within a short period of time.

To summarize, the effects observed in our images include significant edge effects due to global image shift and what seems to be global intensity shading mixed with other susceptibility effects. Because susceptibility effects scale with field, those shifts are expected to be more extreme than those observed in Raj et al.'s study at 1.5T. It is possible that the higher magnetic field strength could play a role in the shading differences as well (global intensity shading vs. intensity gradients). This could be due to experimental differences (field strength, patient orientation, long vs. short bore magnet, etc.) that are impossible to directly compare here.

Further investigation is needed to draw firm conclusions from this data. Specifically, phase maps would be very useful in determining susceptibility-related losses in phase coherence. Unfortunately, the data sets we had were only magnitude images, so calculating phase maps was not possible this time.

APPENDIX B

SIGNAL DISCREPENCIES BETWEEN ACQUISITIONS WITH AND WITHOUT SENSE

Power spectra for studies acquired with SENSE revealed significant (50%) drops in total and respiratory power relative to No Sense. This is not evident from fractional respiratory power values; the ratio behaves consistently across No Sense and SENSE conditions. This may be related to the way SENSE images are acquired or reconstructed, as this is a systematic effect which appears in every acquisition, across every subject, regardless of breath-hold phase encode direction. Currently we have no explanation for these phenomena, but further investigation is underway.

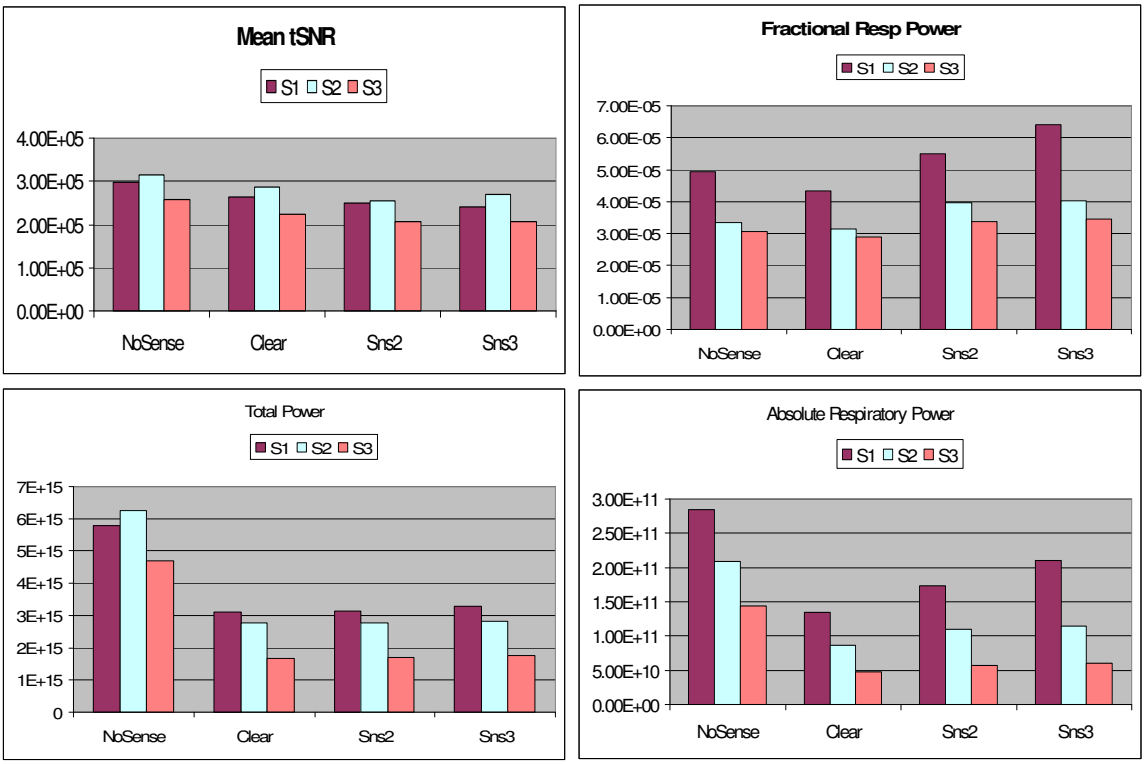

Figure 53. Relative contribution of fractional respiratory power to tSNR for an AP normal breathing acquisition. Both absolute respiratory power and total power are significantly decreased by the application of SENSE, but their ratio continues to increase.

REFERENCES

Biswal B, DeYoe E, Hyde J. Reduction of physiological fluctuations in fMRI using digital filters. MRM. 35 (1996) 107-113.

Biswal B et al. Removal of physiological fluctuations from functional MRI signals. Proc, SMR, 2nd Annual Mtg. San Francisco. 1994. 653.

Chuang K and Chen J. IMPACT: Image-based physiological artifacts estimation and correction technique for functional MRI. MRM. 46 (2001) 344-353.

De Zwart J, et al. Application of sensitivity-encoded echo-planar imaging for blood oxygen level-dependent functional brain imaging. MRM. 48 (2002) 1011-1020.

De Panfilis C and Schwarzbauer C. Positive or negative blips? The effect of phase encoding on susceptibility-induced signal losses in EPI. Neuroimage. 25 (2005) 112-121.

Denolin & Metens. On the calculation and interpretation of signal intensity in echo-shifted sequences. Mag. Res. Med. 51 (2004) 123-134.

Glover G, Pelc N. in 'Magnetic Resonance Annual 1988'. Raven Press, New York, 1988. 299-333.

Glover G, Li T, Ress D. Image-based method for retrospective correction of physiological motion effects in fMRI: RETROICOR. MRM. 44 (2000) 163-167.

Golay et al. PRESTO-SENSE: An ultrafast whole-brain fMRI technique. Mag. Res. Med. 43 (2000) 779-786.

Haacke et al. John Wiley & Sons, NY. 1999. Magnetic Resonance Imaging: Physical Principles and Sequence Design.

Hu X, Kim S. Reduction of physiological noise in functional MRI using Navigator Echo. Magn Reson. Med. 31. (1994) 495-503.

Hu X, et al. Retrospective estimation and correction of physiological fluctuation in Functional MRI. MRM. 34 (1995) 201-212.

Kruger, G et al. Neuroimaging at 1.5T and 3.0T: Comparison of oxygenation-sensitive magnetic resonance imaging. MRM. 45 (2001) 595-604.

Le T and Hu X. Retrospective estimation and correction of physiological artifacts in fMRI by direct extraction of physiological activity from MR data. MRM. 35 (1996) 290-298.

Lin F, et al. Parallel imaging reconstruction using automatic regularization. MRM. 51 (2004) 559-567.

Lin F, et al. Functional MRI using regularized parallel acquisition. MRM. 54 (2005) 343-353.

Liu et al. Mag. Res. Med. Fast echo-shifted gradient-recalled MRI: combining a short repetition time with variable T2* weighting. 30 (1993) 68-75.

Liu et al. A functional MRI technique combining principles of echo-shifting with a train of observations (PRESTO). Mag. Res. Med. 30 (1993) 764-768.

Long C, et al. Nonstationary noise estimation in functional MRI. Neuroimage. 28 (2005) 890-903.

Moeller S, et al. Application of parallel imaging to fMRI at 7 Tesla using a high 1D reduction factor. MRM. 56 (2006) 118-129.

Moonen et al. Functional brain MR imaging based on bolus tracking with a fast T2* sensitized gradient-echo method. Mag. Res. Img. 12 (1994) 379-385.

Moonen et al. A fast gradient-recalled MRI technique with increased sensitivity to dynamic susceptibility effects. Mag. Res. Med. 26 (1992) 184-189.

Nitz, WR. Fast and ultrafast non-echo-planar MR imaging techniques. Eur. Radiol. 12 (2002) 2866-2882.

Noll D, Schneider W. Theory, simulation, and compensation of physiological motion artifacts in functional MRI. Proc. 1st IEEE Conference on Image Processing, Austin, Texas. 1994. 40-44.

Noll D, Schneider W. Respiration artifacts in functional brain imaging: sources of signal variation and compensation strategies. Proc. SMR, 2nd Annual Mtg. San Francisco. 1994. 647.

Pfeuffer J, et al. Correction of physiologically induced global off-resonance effects in dynamic echo-planar spiral functional imaging. MRM. 47 (2002) 344-353.

Preibisch C, et al. Functional MRI using sensitivity-encoding echo planar imaging (SENSE-EPI). NeuroImage 19 (2003) 412-421.

Pruessmann K, et al. SENSE: Sensitivity encoding for fast MRI. MRM 42 (1999) 952-962.

Raj D, et al. A model for susceptibility artifacts from respiration in functional echo-planar magnetic resonance imaging. Phys. Med. Biol. 45 (2000) 3809-3820.

Raj D, Anderson A, Gore J. Respiratory effects in human functional magnetic resonance imaging due to bulk susceptibility changes. Phys. Med. Biol. 46 (2001) 3331-3340.

Schmidt C, et al. Sensitivity-encoded (SENSE) echo planar fMRI at 3T in the medial temporal lobe. NeuroImage. (2005) 25:625-641.

Sekihara K. Steady-state magnetizations in rapid NMR imaging using small flip angles and short repetition intervals. IEEE Trans Med. Img. 6 (1987) 157-164.

Song A. Single-shot EPI with signal recovery from the susceptibility-induced losses. MRM. 46 (2001) 407-411.

Triantafyllou C, et al. Comparison of physiological noise at 1.5 T, 3 T and 7 T, and optimization of fMRI acquisition parameters. Neuroimage. 26 (2005) 243-250.

Troung T, et al. Effects of static and radiofrequency magnetic field inhomogeneity in ultra-high field magnetic resonance imaging. MRI. 24 (2006) 103-112.

Van de Moortele P, et al. Respiration-induced B0 fluctuations and their spatial distribution in the human brain at 7 Tesla. MRM. 47 (2002) 888-895.

Webb, A. *Introduction to Biomedical Imaging*. Wiley & Sons. IEEE Press, Published by John Wiley & Sons, Inc., Hoboken, New Jersey. 2003.

Weisskoff et al. Power spectrum analysis of functionally weighted MR data: What's in the Noise? Proc Soc Magn. Reson. Med (1993) 9:7

Weiskopf N, et al. Optimal EPI parameters for reduction of susceptibility-induced BOLD sensitivity losses: A Whole-brain analysis at 3T and 1.5T. Neuroimage. Article in Press.

Wowk B, McIntyre M, Saunders J. k-Space detection and correction of physiological artifacts in fMRI. MRM. 38 (1997) 1029-1034.

Zhang X, Yacoub E, Hu X. New strategy for reconstructing partial-fourier imaging data in functional MRI. MRM. 46 (2001) 1045-1048.

Zhao Y, Anderson A, Gore J. Computer simulation studies of the effects of dynamic shimming on susceptibility artifacts in EPI at high field. J. Mag. Res. 173 (2005) 10-22.